Plasma Instabilities and Transport in the MPD Thruster

Final Technical Report
AFOSR Contract No. AFOSR-91-0162

Prepared by

Edgar Y. Choueiri, Arnold J. Kelly and Robert G. Jahn,
Electric Propulsion and Plasma Dynamics Lab. (EPPDyL)
Princeton University

Work covering grant period: Feb. 1st 1991 to Feb. 1st 1993

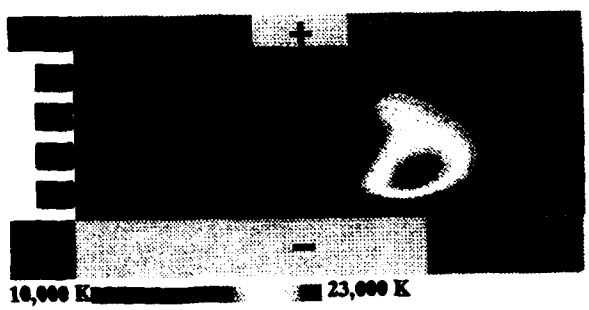

*Original contains color plates: All DTIC reproductions will be in black and white.

AFOSR-TR- 93 0569

DISCLAIMER NOTICE

THIS DOCUMENT IS BEST QUALITY AVAILABLE. THE COPY FURNISHED TO DTIC CONTAINED A SIGNIFICANT NUMBER OF COLOR PAGES WHICH DO NOT REPRODUCE LEGIBLY ON BLACK AND WHITE MICROFICHE.

REPORT DOCUMENTATION PAGE

Form Approved
OMB No 0704-0188

1. AGENCY USE ONLY (Leave blank)	2. REPORT DATE	3. REPORT TYPE AND DATES COVERED
	June 1993	Final Technical Report

4. TITLE AND SUBTITLE

Plasma Instabilities and Transport in the MPD Thruster (u)

5. FUNDING NUMBERS

PE- 61102F
PR- 2308
SA- AS
G- AFOSR-91-0162

6. AUTHOR(S)

Arnold J. Kelly
Edgar Y. Choueiri and Robert G. Jahn

7. PERFORMING ORGANIZATION NAME(S) AND ADDRESS(ES)

Electric Propulsion and Plasma Dynamics Lab (EPPDyL)
MAE Dept, E-Quad
Princeton University
Princeton NJ 08544

8. PERFORMING ORGANIZATION REPORT NUMBER

AFOSR 930569

9. SPONSORING/MONITORING AGENCY NAME(S) AND ADDRESS(ES)

AFOSR/NA
110 Duncan Avenue Suite B115
Bolling AFB DC 20332-0001

10. SPONSORING/MONITORING AGENCY REPORT NUMBER

11. SUPPLEMENTARY NOTES

12a. DISTRIBUTION/AVAILABILITY STATEMENT

Approved for public release; distribution is unlimited

12b. DISTRIBUTION CODE

13. ABSTRACT (Maximum 200 words)

This study deals with the development and testing of anomalous (turbulent) transport coefficient models that include the effects of plasma turbulence and that can be used in plasma fluid codes for more realistic numerical simulations. The anomalous transport models were derived using a kinetic description of microinstabilities in the MPD thruste plasma. Nonlinear plasma theory was used under the valid approximation of weak turbulenc and the resulting transport models were studied in detail.A strong dependence of anomalous transport on the electron Hall parameter was found. The models were then reduced to a set of compact polynomials ideally suited for inclusion in fluid codes. The usefulness and importance of these models were demonstrated by including them in an advanced plasma fluid code and carrying numerical simulations of realistic MPD thruster flows. The results show the impact of turbulence on various aspects of dissipation in the thruster as well as on the overall propulsive efficeincy. Fluid codes that include these models are more accurate engineering tools for the design and study of high efficiency plasma thrusters.

14. SUBJECT TERMS

MPD Thrusters, Electric Propulsion, Plasma Instabilities, Plasma Turbulence, Anomalous Transport, Fluid Simulation

15. NUMBER OF PAGES

50

16. PRICE CODE

17. SECURITY CLASSIFICATION OF REPORT	18. SECURITY CLASSIFICATION OF THIS PAGE	19. SECURITY CLASSIFICATION OF ABSTRACT	20. LIMITATION OF ABSTRACT
Unclassified	Unclassified	Unclassified	UL

Contents

1 Abstract or Summary **2**

2 Background **3**
2.1 Project and Final Report Description 3
2.2 Report Organization 3
2.3 Relevance 3

3 Anomalous Transport Models for the MPD Thrsuter Plasma **5**
3.1 Methodolgy 5
3.2 Weak Turbulence Kinetic Formalism for Anomalous Transport . 6
3.3 Governing Equations 7
3.3.1 The Moment-Generating Equation 7
3.3.2 Evolution of Average Macroscopic Properties under Microturbulence 8
3.4 Momentum Exchange and Heating Rates 9
3.5 Saturation Mechanisms 17
3.6 Thermodynamic Limit: The Fowler Bound 18
3.6.1 Saturation by Ion Trapping 18
3.6.2 Saturation by Electron Trapping 18
3.6.3 Saturation by Resonance Broadening 19
3.7 Calculations of Anomalous Transport 19
3.7.1 Classical Benchmarks 19
3.7.2 Numerical Results 20
3.7.3 MPD Thruster Calculations 27

4 Anomalous Transport Models and their Inclusion in Fluid Codes **29**
4.1 Goals 29
4.2 Final Models 29
4.3 Fluid Code Description 32
4.4 Results 33
4.4.1 Discussion of Performance Curves 33
4.4.2 Current Distribution 36
4.4.3 Comparison Between a Classical and an Anomalous Run for High Current 37

5 Conclusions **40**

6 Appendix **44**

7 Non-technical Material **45**
7.1 Publications supported by the AFOSR Grant 45
7.2 Particpating Professionals 46
7.3 Advanced Degrees 46
7.4 Professional Interactions 46
7.5 Other Relevant Information 46

Plasma Instabilities and Transport in the MPD Thruster

Final Technical Report
AFOSR Contract No. AFOSR-91-0162

Prepared by

Edgar Y. Choueiri, Arnold J. Kelly and Robert G. Jahn,
Electric Propulsion and Plasma Dynamics Lab. (EPPDyL)
Princeton University

Work covering grant period: Feb. 1st 1991 to Feb. 1st 1993

1 Abstract or Summary

This study aims at developing and testing anomalous (turbulent) transport coefficient models that include the effects of plasma turbulence and that can be used in more realistic numerical simulations of MPD thruster flows. The anomalous coefficients were derived using a kinetic description of microinstabilities in the finite-beta, magnetized, collisonal and flowing plasma of the MPD thruster. Nonlinear plasma theory was used under the valid approximation of weak turbulence. The resulting transport models were studied in detail in the parameter-space corresponding to typical MPD thruster operation and a strong dependence of anomalous transport on the electron Hall parameter was found. The models were than reduced to a set of compact polynomials ideally suited for self-consitent fluid flow calculations. The usefulness and value of these models were demonstrated by including them in an advanced plasma fluid code and carrying numerical simulations of realistic MPD thruster flows. The results show the impact of turbulence on various aspects of dissipation in the thruster as well as on the overall propulsive efficiency.

2 Background

2.1 Project and Final Report Description

In this final report we present the final results of a two-year theoretical and numerical study in which we developed and tested transport coefficient models that include the effects of plasma turbulence. The resulting anomalous transport models are intended to be included in fluid codes thus rendering more realistic the numerical simulations of MPD thruster[1] flows.

Computer models of the MPD thruster rely on the numerical solution of the magnetohydrodynamics (MHD) equations to predict the performance and aid in the design of higher efficiency thrusters. Current MHD models of the accelerator include only classical transport[2] (i.e. transport due to collisions between particles) and overpredict the performance of the experimental prototypes. The inclusion of anomalous transport (i.e. transport due to "collisions" of particles with the oscillating fields of unstable waves in the plasma) is expected to greatly enhance the validity and applicability of such models. During the past year our reserach has produced a first generation of transport coefficient models that can be readily included in any plasma fluid code computer code.

2.2 Report Organization

This final report documents the entire work starting with its relevance to the design of high efficiency plasma thrusters for spacecraft propulsion, the methodology behind the approach, the derivation of the anomalous transport models, a description of how they are to be used in a standard fluid flow code and ending with actual numerical simulations of MPD thrsuter flows using the models in an advanced plasma fluid code developed at our laboratory.

Non-technical information related to the grant and the work it supported is given at the end of this report.

2.3 Relevance

The ultimate goal of MPD thruster research is the development of high-efficiency long lifetime plasma thrusters that can be used for energetic spacecraft propulsion requirements[3].

The current performance of MPD thrusters is limited to modest efficiencies (below 30% for argon) and plasma fluid computer codes (which are the ultimate non-experimetal tools for studying thruster design problems) are handicaped

[1]Throughout this report the term MPD thruster refers to the coaxial, self-field, high-current, gas-fed MagnetoPlasmaDynamic thruster.

[2]Throughout this report, "transport" refers to the following processes: electrical conductivity, particle diffusion, viscosity and thermal conductivity.

[3]By "energetic" we mean missions that require high increment in spacecraft velocity, Δv (delta vee) such as orbit raising, some demanding attitude control situations and interplanetary propulsion.

by the absence of the representation of some crucial physics. Notably, all codes in use today cannot account for the effects of plasma turbulence caused by microintsbailies in the plasma. The reason such turbulent effects are important is that can strongly enhance heating and ionization of the plasma. Heating and ionization are essentially dissipative processes for the MPD thruster because the flow is practically frozen and the energy invested in them is very difficult to recuperate as propulsive thrust.

Our work previous to this AFOSR-sponsored project[1, 2, 3, 4] has shown that the MPD thruster is a plasma accelerator whose performance is dictated by the competition between current-driven acceleration, which constitutes the prime acceleration mechanism in the device, and current-driven dissipation. Current-driven acceleration makes the MPD thruster a prime candidate for spacecraft propulsion while, current-driven dissipation is a handicap that must be surmounted if these devices are to be of practical use. This competition between two processes driven by the same source, the current, is manifested in the low thrust efficiency of the present devices.

The high-current acceleration of a plasma can be explained, on the kinetic level, as primarily due to the transfer of momentum from the current-carrying electrons to the ion gas through long-range (Coulomb) collisions. Alternatively, on the macroscopic level, the bulk plasma acceleration can be viewed as the result of the action of the Lorentz body force on the bulk plasma. The Lorentz force is due to the interaction of the current carried by the electrons with the induced magnetic field.

On the other hand, the same current is responsible for enhanced (turbulent) transport associated with current-driven plasma instabilities. As is well known from plasma physics, any current having an associated drift velocity exceeding the thermal velocity of one of the charged species represents a potential free source of energy that can effectively excite one or more of the many natural plasma wave modes into unstable growth. For the MPD accelerator, the nature of the current (its transversality to the magnetic field), the magnitude of its associated drift velocity u_{de} compared to the ion thermal velocity v_{ti}, and the plasma parameters are such that a current-driven instability (related to a finite-beta collisional lower hybrid oscillations) is naturally excited.

This current-driven plasma instability has the peculiarity of anisotropic electron heating which means that fast electrons are preferentially heated along the magnetic field lines. Such production of suprathermal electrons by the instability usually translates into a substantial enhancement in ionization (over-ionization) since the ionization process in the MPD thruster is primarily due to electron impact i.e. collisions between energetic electrons and neutrals. Similarly, the populations of excited states are enhanced (excitation) through the same process.

Plasma heating, excitation and over-ionization are not desirable in the MPD accelerator since the time scales for enthalpy recovery (conditioned by the reverse processes: cooling, deexcitation and recombination) are much longer

than the plasma residence time. The translational, internal and chemical modes are in a strongly non-equilibrium state, or equivalently the flow is frozen with respect to these modes primarily because of the low particle densities that are associated with the operation of MPD devices at reasonable power levels. In other words, the low density typical of MPD thrusters limits the collisional equilibration and recuperation of the energy tied in the random kinetic, internal and chemical modes which become unavailable to the propulsive action of the plasma. Thruster efficiency is thus degraded.

The work documented here aims at developing models for the anomalous transport caused by plasma microinstabilities as well as at the testing of these models in actual plasma fluid codes. We start with the derivation of these models.

3 Anomalous Transport Models for the MPD Thrsuter Plasma

3.1 Methodolgy

We start by using the linear stability description that we have developed in work prior to this AFOSR-sponsored project[3, 4] along with plasma weak turbulence theory to develop a second order description of wave-particle transport and anomalous dissipation.

In Sections 3.2 and 3.3 we outline the basic formalism we adopt for our formulation of anomalous transport. In Section 3.4 we use the statistical description of the previous section to derive general *finite-beta* expressions for the anomalous ion and electron heating rates as well as for the electron-wave momentum exchange rate that controls the anomalous resistivity effect. These expressions are cast as integrals in wavevector space of quantities that depend on the various elements of the linear dispersion tensor derived in detail in [5], on the roots of the linear dispersion relation and on the saturation energy density of the fluctuating (turbulent) fields denoted by $\mathcal{E}_t$.

We then turn our attention in Section 3.5 to the difficult question of the saturation mechanism that dictates the magnitude and dependencies of $\mathcal{E}_t$. We consider four models for $\mathcal{E}_t$ based on four possible saturation mechanisms.

In Section 3.7 we show various calculations of the anomalous heating and momentum exchange rates for plasma parameters of interest and compare their magnitudes to classical values.

We finally conclude the analysis of anomalous transport in Section 4 by using these calculations to arrive at polynomial expressions of the relevant transport coefficients cast solely in terms of macroscopic parameters for inclusion in plasma fluid codes of the accelerator.

These polynomials are then ready for use in a fluid code as described in the rest of the report.

3.2 Weak Turbulence Kinetic Formalism for Anomalous Transport

The kinetic theory of weak turbulence was first developed by *Vedenov, Velikhov and Sagdeev*[6] (1961) as well as *Drummond, Pines and Rosenbluth* [7] (1962). Its current status is probably best exposed by *Galeev and Sagdeev* in ref. [8] (1982). The theory allows for far deeper insight into the description of turbulent transport than that afforded by the hydrodynamic theory of turbulence. This is due to the fact that, unlike a neutral fluid where turbulence is synonymous with strong nonlinear couplings, plasma microturbulence is often characterized by primarily *linear* interactions between unstable modes superimposed on small amplitude nonlinearly induced waves[9, p. 289].

Formally, the validity of the weak turbulence theory hinges on the smallness of the ratio of the fluctuating energy density to the plasma thermal energy density

$$\frac{\mathcal{E}_t}{\sum_s n_s T_s} \ll 1, \tag{1}$$

where n_s and T_s are the density and temperature of species s. We shall find it more convenient in the following sections to deal with the ratio $\mathcal{E}_t/n_0 T_i$, (n_0 representing the background charged particle density) which is very close to the above ratio for a quasi-equithermal plasma. It is possible to relate the weak turbulence scaling parameter $\mathcal{E}_t/n_0 T_i$ to the experimentally measurable density fluctuation $\tilde{n}/n_0$, where the tilde denotes a fluctuating quantity by noting that $\tilde{n}/n_0 \approx e\tilde{\phi}/T_e$ and $\epsilon\tilde{\phi} \approx e\tilde{E}/k$ (where e is the electron charge, $\tilde{\phi}$ the wave potential, k the wavenumber or the magnitude of the wavevector $\boldsymbol{k}$ and E the electric field) so that

$$\frac{\mathcal{E}_t}{n_0 T_i} \approx \frac{T_e}{T_i} \frac{(k r_{ce})^2}{4} \left(\frac{\tilde{n}}{n_0} \Big|_{rms} \right)^2. \tag{2}$$

Experimental evidence of turbulent fluctuations caused by cross-field current-driven instabilities was recently found in the low-power steady-state MPD thruster plasma at various conditions and locations in the plume[10, 11]. These measured turbulent fluctuations had most of their power in the lower hybrid mode with some power appearing sometimes in the electron cyclotron harmonics. Measured values of $(\tilde{n}/n_0)_{rms}$ when such turbulence was observed were on the order of .1 with magnitudes ranging between .05 and .7. For these values, with $1 \geq T_i/T_e \leq 6$, $\mathcal{E}_t = \epsilon_0 |\tilde{E}_k|^2/2$ (where ϵ_0 is the permittivity of free space and r_{ce} is the electron cyclotron radius) and assuming $(k r_{ce})^{**} \approx .1$[5], we obtain from Eq. (2) an estimate for $\mathcal{E}_t/n_0 T_i$ ranging between 10^{-3} and 10^{-6} implying that the weak turbulence assumption is generally valid.

One of the most fortunate turn of events in modern plasma physics has been the surprising ability of weak turbulence theory to describe experimental obser-

vations even for fairly large amplitude waves[9, p. 291]. A historical perspective on the evolution of the formalism is given in [5, pp. 118-119].

3.3 Governing Equations

3.3.1 The Moment-Generating Equation

In this sub-section we present an outline of the derivation of the general form of fluid-like equations governing the evolution of macroscopic quantities under the conditions of weak turbulence. Detailed discussions of such a derivation have already been presented in numerous articles (see refs. [12, 13], for instance, for a tutorial review). We do this in preparation to our derivation of anomalous transport presented in the following sections.

We should mention at the outset that our interest lies not in the evolution equation itself but rather in its use as a moment-generating equation. Therefore, for the sake of simplicity and in order to keep a connection with the literature, we shall neglect collisions in the kinetic evolution equation. The effects of collisions will be reintroduced later when we use the explicit form of the dispersion tensor elements.

The underlying idea is to consider the distribution function of the s species, f_s, as the sum of a slowly varying ensemble-average part and a rapidly varying fluctuating part

$$f_s(\boldsymbol{x}, \boldsymbol{v}, t) = F_s(\boldsymbol{v}, t) + \tilde{f}_s(\boldsymbol{x}, \boldsymbol{v}, t) \tag{3}$$

where $F_s(\boldsymbol{v}, t) = \langle f_s(\boldsymbol{x}, \boldsymbol{v}, t) \rangle$ and $\langle \quad \rangle$ denotes an ensemble-average[14] while the tilde denotes a quantity fluctuating due to the effects of unstable waves. When similar partitions are effected on the electric and magnetic field vectors, the kinetic (Vlasov) equation for a spatially uniform equilibrium yields

$$\begin{aligned} \frac{\partial F_s}{\partial t} - \omega_{cs}\frac{\partial F_s}{\partial \phi} + \frac{q_s}{m_s}\left[\tilde{\boldsymbol{E}} + \boldsymbol{v} \times \tilde{\boldsymbol{B}}\right] \cdot \nabla_v F_s = \\ -\left(\frac{\partial \tilde{f}_s}{\partial t} + \boldsymbol{v} \cdot \nabla \tilde{f}_s - \omega_{cs}\frac{\partial \tilde{f}_s}{\partial \phi}\right. \\ \left. + \frac{q_s}{m_s}\left[\tilde{\boldsymbol{E}} + \boldsymbol{v} \times \tilde{\boldsymbol{B}}\right] \cdot \nabla_v \tilde{f}_s\right) \end{aligned} \tag{4}$$

where q_s, m_s, ω_{cs} are charge, mass and cyclotron frequency of species s and where we have chosen to work with the cylindrical phase space coordinates $v_\perp, \phi, v_z$ (representing the velocity perpendicular to the magnetic field $\boldsymbol{B}$, the cylindrical angle and the parallel velocity, the magnetic field being aligned with the z-axis). Taking the ensemble-average of the above equation, while noting that $\langle \tilde{f}_s \rangle = 0$, results in

$$\frac{\partial F_s}{\partial t} - \omega_{cs}\frac{\partial F_s}{\partial \phi} = \left(\frac{\partial F_s}{\partial t}\right)_{AN} \tag{5}$$

where the right hand side represents the anomalous contribution that is the response of the average distribution function to the microturbulent fluctuations and can be written explicitly as

$$\left(\frac{\partial F_s}{\partial t}\right)_{AN} = \left\langle -\frac{q_s}{m_s}\left[\tilde{\boldsymbol{E}} + v \times \tilde{\boldsymbol{B}}\right] \cdot \nabla_v \tilde{f}_s \right\rangle. \tag{6}$$

By subtracting Eq. (6) from Eq. (4) and, in the spirit of weak turbulence theory, neglecting all terms that are quadratic in the fluctuation amplitude (which is tantamount to the neglect of *nonlinear* wave-particle and wave-wave interactions) the following governing equation is obtained for a weakly turbulent plasma

$$\frac{\partial \tilde{f}_s}{\partial t} + v \cdot \nabla \tilde{f}_s - \omega_{cs}\frac{\partial \tilde{f}_s}{\partial \phi} = -\frac{q_s}{m_s}\left[\tilde{\boldsymbol{E}} + v \times \tilde{\boldsymbol{B}}\right] \cdot \nabla_v F_s. \tag{7}$$

The standard procedure in weak turbulence theory (expounded in ref. [14] for instance) is to solve Eq. (7) along with Maxwell's equations for $\tilde{\boldsymbol{E}}, \tilde{\boldsymbol{B}}$ and $\tilde{f}_s$ then substitute the result into Eq. (5) to obtain the evolution of F_s in the presence of microturbulence. We shall not, however, need to do all that for our particular problem of deriving expressions for the momentum and energy exchange rates. Such expressions can be arrived at by taking moments of the governing equation (Eq. (5)) as outlined below.

3.3.2 Evolution of Average Macroscopic Properties under Microturbulence

To obtain the macroscopic evolution equations we take moments of Eq. (5) *i.e.* we multiply the equation by the generic quantity of transport Θ (which could represent mass, momentum or energy) and integrate over velocity space to get

$$\frac{\partial}{\partial t}\int \Theta F_s d\,v - q_s m_s \int (v \times \boldsymbol{B}_0 \cdot \nabla_v \Theta)\, F_s\, dv = \frac{q_s}{m_s}\left\langle \int \left[\left(\tilde{\boldsymbol{E}} + v \times \tilde{\boldsymbol{B}}\right) \cdot \nabla_v \Theta\right] \tilde{f}_s\, dv \right\rangle \tag{8}$$

where we have used integration by parts in order to move the distribution functions outside the operators. Taking successive moments of Eq. (5) is equivalent to substituting $\Theta = 1, v, vv$ (for mass, momentum and energy respectively) in Eq. (8) and integrating over v-space. This yields

$$\frac{\partial \langle n_s \rangle}{\partial t} = 0 \tag{9}$$

$$\frac{\partial \langle \boldsymbol{\Gamma}_s \rangle}{\partial t} + (\omega_{cs}\boldsymbol{e}_z) \times \langle \boldsymbol{\Gamma}_s \rangle = \frac{q_s}{m_s}\left\langle \tilde{\boldsymbol{E}}\tilde{n}_s + \tilde{\boldsymbol{\Gamma}}_s \times \tilde{\boldsymbol{B}} \right\rangle \tag{10}$$

$$\frac{\partial \langle \boldsymbol{W}_s \rangle}{\partial t} + 2(\omega_{cs}\boldsymbol{e}_z) \times \langle \boldsymbol{W}_s \rangle = 2\frac{q_s}{m_s}\left\langle \tilde{\boldsymbol{E}}\tilde{\boldsymbol{\Gamma}}_s + \tilde{\boldsymbol{W}}_s \times \tilde{\boldsymbol{B}} \right\rangle \tag{11}$$

where $\boldsymbol{e}_z$ is the unit vector along the z-axis, and we have used the following definitions

$$n_s = \int f_s \, dv \tag{12}$$

$$\boldsymbol{\Gamma}_s = n_s \boldsymbol{v}_{ds} = \int \boldsymbol{v} f_s \, dv \tag{13}$$

$$\boldsymbol{W}_s = m_s \int \boldsymbol{v}\boldsymbol{v} f_s \, dv \tag{14}$$

for the average number density, the particle flux density and the kinetic energy density tensor, respectively (with $\boldsymbol{v}_{ds}$ as the drift velocity vector of species s).

3.4 Momentum Exchange and Heating Rates

We now proceed to define and derive explicit relations for the anomalous rates of interest.

The right hand side of Eq. (10) represents the rate of momentum exchange $(\partial \boldsymbol{P}_s/\partial t)_{AN}$ (where the momentum density vector is $\boldsymbol{P}_s = m_s \boldsymbol{\Gamma}_s$) between the particles and the fluctuating fields. Since we shall be interested in the momentum exchange along the drift velocity vector, we write

$$\left(\frac{\partial \boldsymbol{P}_s}{\partial t}\right)_{AN} \cdot \boldsymbol{v}_{ds} = -\left(\nu_s^p\right)_{AN} \boldsymbol{P}_s \cdot \boldsymbol{v}_{ds} \tag{15}$$

where we have defined $(\nu_s^p)_{AN}$ as the effective anomalous momentum exchange rate (or frequency) between species s and the fluctuating fields. Using the explicit expression for $(\partial \boldsymbol{P}_s/\partial t)_{AN}$ from Eq. (10) in the above equation we obtain

$$\left(\nu_s^p\right)_{AN} = -\frac{q_s}{n_s m_s v_{ds}}\left\langle \frac{\tilde{\boldsymbol{E}} \cdot \boldsymbol{v}_{ds}\tilde{n}_s}{v_{ds}} + \frac{\boldsymbol{v}_{ds} \cdot (\tilde{\boldsymbol{\Gamma}}_s \times \tilde{\boldsymbol{B}})}{v_{ds}} \right\rangle \tag{16}$$

where, unlike most derivations in the literature, we are retaining the full electromagnetic character of the microturbulence.

We now specialize the above expression for our particular problem according to the MPD thruster configuration shown in Fig. (1). We thus obtain the effective anomalous momentum exchange rate for electrons along the current after setting $s = e$, staying in the ion reference frame and aligning the relative drift u_{de} along the y-axis,

$$\left(\nu_e^p\right)_{AN} = \frac{e}{n_0 m_e u_{de}}\left\langle \tilde{E}_y \tilde{n}_e + n_0 \tilde{u}_{de_z} \tilde{B}_x - n_0 \tilde{u}_{de_x} \tilde{B}_z \right\rangle \tag{17}$$

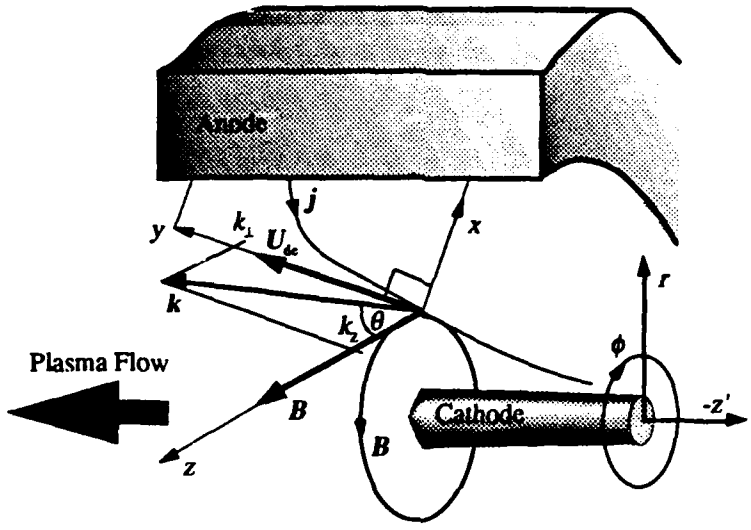

Figure 1: The vectors j, B, k and u_{de} in the local cartesian coordinate frame. Also shown is the accelerator's fixed cylindrical coordinate frame, r-z'-θ.

where we have used the relation $\tilde{\Gamma}_s = \tilde{n}_s v_{ds} + n_0 \tilde{v}_{ds}$.

The frequency $(\nu_e^p)_{AN}$ can be thought of as an effective "collision" frequency between the electrons and the fluctuating fields and can thus be associated with a resistivity called "anomalous resistivity" the same way that the coulomb collision frequency ν_{ei} is associated with the classical Spitzer resistivity. By analogy the anomalous resistivity $(\eta)_{AN}$ is proportional to $(\nu_e^p)_{AN}$ and is given by

$$(\eta)_{AN} = \frac{m_e (\nu_e^p)_{AN}}{n_0 e^2}. \tag{18}$$

The effective collision frequency $(\nu_e^p)_{AN}$ is therefore a direct measure of anomalous resistivity.

Similarly, for the temperature

$$T_s = \frac{m_s}{3n_s} \int (v - v_{ds})^2 f_s \, dv \tag{19}$$

we define a heating rate for species s by

$$\nu_s^T \equiv \frac{1}{T_s} \frac{\partial T_s}{\partial t} \tag{20}$$

and obtain, after combining Eqs. (10) and (11) and specializing for the MPD thruster configuration,

$$(\nu_i^T)_{AN} = \frac{2e}{3n_0 T_i} \left\langle n_0 \tilde{E} \cdot \tilde{u}_{di} \right\rangle \tag{21}$$

for the ions and

$$\begin{aligned}\left(\nu_e^T\right)_{AN} &= \frac{-2e}{3n_0T_e}\Big\langle n_0\tilde{E}\cdot\tilde{u}_{de} \\ &- n_0u_{de}\left(\tilde{u}_{de_r}\tilde{B}_z-\tilde{u}_{de_z}\tilde{B}_r\right)\Big\rangle \end{aligned} \tag{22}$$

for the electrons.

Eqs. (17), (21) and (22) will be the focus of our remaining analysis and calculations.

In order to proceed with more useful forms for these expressions we need to eliminate the fluctuating density, velocity and magnetic field in favor of the fluctuating electric field. For this purpose we invoke, in the spirit of a quasilinear description, relations between the fluctuating quantities and the fluctuating electric field that follow those of their linearly oscillating counterparts. From a generalized Ohm's law we can write for species s[4]

$$\tilde{j}_{s_k} = -i\epsilon_0\omega\boldsymbol{R}^{(s)}\tilde{E}_k \tag{23}$$

(where j is the current density, $\boldsymbol{R}^{(s)}$ is the dispersion tensor of species s and ω is the wave frequency) which, combined with the continuity relation[4]

$$n_s^{(1)} = \frac{\boldsymbol{k}\cdot\boldsymbol{j}_s^{(1)}}{\omega q_s}, \tag{24}$$

gives a useful expression for the fluctuating density of species s

$$\tilde{n}_{s_k} = \frac{\boldsymbol{k}\cdot\tilde{\boldsymbol{j}}_s}{\omega q_s} = -i\frac{\epsilon_0}{q_s}\sum_l k_l\sum_m R_{lm}^{(s)}\tilde{E}_{m_k} \tag{25}$$

where the subscript k is a reminder that these relations are for the spectrally resolved (*i.e.* Fourier transformed) fluctuations. In this expression, $R_{lm}^{(s)}$ are the elements of the tensor representing the dielectric response of species s and can be readily obtained from Eqs. (90)-(97) (derived in[5] and quoted in the appendix) through transformations that will be described further below.

In a similar fashion we can derive an expression for $\tilde{u}_{ds}$ from the following relation

$$\tilde{\boldsymbol{j}}_s = q_s\left(n_0\tilde{\boldsymbol{u}}_{ds}+\tilde{n}_s\boldsymbol{u}_{ds}\right) \tag{26}$$

and Eq. (25), yielding

$$\tilde{\boldsymbol{u}}_{s_k} = -\frac{i\epsilon_0\omega\boldsymbol{R}^{(s)}\tilde{\boldsymbol{E}}_k}{q_sn_0}+\left[i\frac{\epsilon_o}{q_sn_0}\boldsymbol{k}\cdot\left(\boldsymbol{R}^{(s)}\tilde{\boldsymbol{E}}_k\right)\right]\boldsymbol{u}_{ds}. \tag{27}$$

We shall not need to worry about the second term on the right hand side of the above equation in the context of the MPD thruster configuration shown in

Fig. (1), because this term vanishes for the ions ($u_{di} = 0$, having chosen to stay in the ion rest frame) and for the electrons it is also nil for the components that figure in Eqs. (17) and (22) (*i.e.* the x and z components) so that we are left with

$$\tilde{u}_{ds_{l_k}} = -i\frac{\epsilon_o}{q_s n_0}\omega \sum_m R^{(s)}_{lm}\tilde{E}_{m_k} \tag{28}$$

where $l = x, z$ for $s = e$; and $l = x, y, z$ for $s = i$.

Having related the fluctuating density and velocity to the fluctuating electric field we need to do the same for $\tilde{\boldsymbol{B}}$. To this end, the following equation

$$\tilde{\boldsymbol{E}} = i\omega\tilde{\boldsymbol{A}} - i\boldsymbol{k}\tilde{\Phi}, \tag{29}$$

which relates the electromagnetic potential $\tilde{\boldsymbol{A}}$ and electrostatic potential $\tilde{\Phi}$ to the electric field $\tilde{\boldsymbol{E}}$ (see our previous study in [4]), gives, for our particular configuration,

$$\tilde{E}_{x_k} = i\omega\tilde{A}_{x_k} \tag{30}$$

$$\tilde{E}_{y_k} = -ik_\perp\tilde{\Phi}_k - i\omega\frac{k_x}{k_\perp}\tilde{A}_{x_k} \tag{31}$$

$$\tilde{E}_{z_k} = -ik_z\tilde{\Phi}_k + i\omega\tilde{A}_{z_k} \tag{32}$$

Furthermore, combining the above equations with the definition of the electromagnetic potential,

$$\boldsymbol{B} = \nabla \times \boldsymbol{A}, \tag{33}$$

and Coulomb's gauge, yields the desired relations

$$\tilde{B}_{x_k} = \frac{1}{\omega}\left(k_\perp\tilde{E}_{z_k} - k_z\tilde{E}_{y_k}\right) \tag{34}$$

$$\tilde{B}_{y_k} = \frac{k_x}{\omega}\tilde{E}_{x_k} \tag{35}$$

$$\tilde{B}_{z_k} = -\frac{k_\perp}{\omega}\tilde{E}_{x_k}. \tag{36}$$

We are now in a position to evaluate the terms of Eqs. (17), (22) and (21) by carrying the ensemble-averages using the random phase approximation (which is a standard technique of statistical physics commonly used in the spectral resolution of fluctuations, see Ref. [15, pages 371–373] for instance). For the first term in Eq. (17) using Eq. (25) we have,

$$\left\langle \tilde{E}_y\tilde{n}_e \right\rangle = \left\langle \int\int \frac{i\epsilon_0}{e}\sum_l k_l \sum R^{(e)}_{lm} \times \tilde{E}_{m_k}\tilde{E}_{y'_k}e^{i(\boldsymbol{k}\cdot\boldsymbol{x}+\boldsymbol{k}'\cdot\boldsymbol{x})}\,d\boldsymbol{k}\,\boldsymbol{k}' \right\rangle \tag{37}$$

which yields under the assumption of random phase[4]

$$\left\langle \tilde{E}_y \tilde{n}_e \right\rangle = -\frac{\epsilon_0}{e} \int \Im \left\{ \sum_l k_l \sum_m R^{(e)}_{lm} \tilde{E}_m \tilde{E}_y \right\} d\boldsymbol{k} \tag{38}$$

where $\Im\{\ \}$ denotes the imaginary part of a complex quantity. Similarly, we find for the other two terms in Eq. (17)

$$\left\langle \tilde{u}_{de_z} \tilde{B}_z \right\rangle = -\frac{\epsilon_0}{e} \int \Im \left\{ \left(\sum_m R^{(e)}_{zm} \tilde{E}_m \right) \times \left(k_\perp \tilde{E}_z - k_z \tilde{E}_y \right) \right\} d\boldsymbol{k} \tag{39}$$

$$\left\langle \tilde{u}_{de_z} \tilde{B}_z \right\rangle = \frac{\epsilon_0}{e} \int \Im \left\{ \left(\sum_m R^{(e)}_{zm} \tilde{E}_m \right) \times k_\perp \tilde{E}_z \right\} d\boldsymbol{k}. \tag{40}$$

If we now substitute the above three equations in Eq. (17), expand and collect the terms in the summations while taking advantage of the following symmetry properties of the dispersion tensor

$$R^{(s)}_{xy} = -R^{(s)}_{xy}; \quad R^{(s)}_{xz} = -R^{(s)}_{xz}; \quad R^{(s)}_{yz} = R^{(s)}_{xy}, \tag{41}$$

we arrive at

$$(\nu^p_e)_{AN} = -\frac{\epsilon_0}{u_{de} m_e n_e} \times \int \Im \left\{ k_\perp \left[\left(\sum_l R^{(e)}_{ll} |\tilde{E}_l|^2 \right) + 2R^{(e)}_{yz} |\tilde{E}_y \tilde{E}_z| \right] \right\} d\boldsymbol{k}. \tag{42}$$

We shall find it convenient, for our particular instability, to cast the the above expression in terms of the spectrally resolved fluctuating field energy density in the perpendicular direction, $\mathcal{E}_{k_\perp}$. This can be done by using the following relations obtained from Eq. (41) and the governing equation[4]

$$\boldsymbol{R}\boldsymbol{E}^{(1)} = 0 \tag{43}$$

(where the superscript denotes the oscillating part of the electric field) to yield

$$A \equiv \frac{\tilde{E}_z}{\tilde{E}_y} = \frac{R_{yy} R_{xz} - R_{xy} R_{yz}}{R_{xy} R_{xz} + R_{xz} R_{yz}} \tag{44}$$

[4]From here on, we shall, for the sake of simplicity, drop the subscript k from the fluctuating quantities.

$$B \equiv \frac{\tilde{E}_z}{\tilde{E}_y} = -\frac{R_{xy}R_{zz} - R_{xz}R_{yz}}{R_{xx}R_{zz} + R_{xz}R_{xz}} \tag{45}$$

(where each element R_{lm} is the sum of the corresponding contributions from the electrons, ions and vacuum) to eliminate $\tilde{E}_x$ and $\tilde{E}_z$ and give

$$\begin{aligned}(\nu_e^p)_{AN} = &-\frac{2}{u_{de} m_e n_e} \int \mathcal{E}_{k_\perp} k_\perp \\ &\times \Im \left\{ R_{xx}^{(e)} A^2 + R_{yy}^{(e)} \right. \\ &\left. + R_{zz}^{(e)} B^2 + 2 R_{yz}^{(e)} B \right\} d\boldsymbol{k}.\end{aligned} \tag{46}$$

We have carried out our derivation above under the electric field formalism where the relevant dispersion tensor is $\boldsymbol{R}$ (*cf* Eq. (43)). The dispersion tensor $\boldsymbol{D}$ that we derived explicitly in [5], however, was obtained under the potential formalism (*cf* Eqn. (30) of ref. [4]). As was the case in that paper, switching to the potential formalism has some advantages. In the context of anomalous transport, the potential formalism allows a more physical insight by expressing the momentum exchange and heating rates in terms of an electrostatic contribution plus a finite-beta correction. The results obtained so far can readily be recast in terms of the elements D_{lm} of Eqs. (90)-(97), through the following linear transformations obtained from combining Eqs. (43), (30), (31) and (32),

$$R_{xx} = D_{22} \tag{47}$$

$$R_{xy} = -R_{yx} = \frac{k_\perp}{k}\left(\frac{k_x}{k} D_{23} - D_{12}\right) \tag{48}$$

$$R_{xz} = -R_{zx} = -\frac{k_\perp^2}{k^2} D_{23} - \frac{k_x}{k} D_{12} \tag{49}$$

$$R_{yy} = \frac{k_\perp^2}{k^2}\left(D_{11} + 2\frac{k_x}{k} D_{13}\right) + \frac{k_x^2}{k^2} D_{33} \tag{50}$$

$$\begin{aligned}R_{yz} = R_{yz} &= \frac{k_\perp}{k}\left[\frac{k_x^2}{k^2} - \frac{k_\perp^2}{k^2}\right] D_{13} \\ &+ \frac{k_\perp k_x}{k^2}\left(D_{11} - D_{33}\right)\end{aligned} \tag{51}$$

$$R_{zz} = \frac{k_\perp^2}{k^2} D_{33} + \frac{k_x^2}{k^2} D_{11} - 2\frac{k_\perp^2}{k^2}\frac{k_x}{k} D_{13}. \tag{52}$$

We also need to separate the contributions of electrons, ions and vacuum in the dispersion tensor, which can be done following

$$D_{lm}^{(e)} = D_{lm} - D_{lm}^{(0)} - D_{lm}^{(i)} \tag{53}$$

where subscripts l and m cover the indices 1, 2 and 3 and where the superscript (0) denotes the contribution of vacuum. The elements $D_{lm}^{(0)}$ and $D_{lm}^{(i)}$ are given

by

$$D_{11}^{(0)} = 1, \quad D_{22}^{(0)} = D_{33}^{(0)} = 1 - N^2$$
$$D_{12}^{(0)} = D_{13}^{(0)} = D_{23}^{(0)} = 0 \tag{54}$$

and

$$D_{11}^{(i)} = \frac{2\omega_{pi}^2}{k^2 v_{t_i}^2}(1 + \zeta_i Z_i) \tag{55}$$

$$D_{22}^{(i)} = D_{33}^{(i)} = \frac{\omega_{pi}^2}{\omega^2}\zeta_i Z_i \tag{56}$$

$$D_{12}^{(i)} = D_{13}^{(i)} = D_{23}^{(i)} = 0. \tag{57}$$

When the above transformations (Eqs. (47)-(57)) are used in Eq. (46) to eliminate $R_{lm}^{(e)}$ in favor of $D_{lm}^{(e)}$, we finally obtain after some straightforward algebra

$$\begin{aligned}(\nu_e^p)_{AN} = [(\nu_e^p)_{AN}]_L - \frac{2}{u_{de} m_e n_e} \int \mathcal{E}_{k_\perp} k_\perp \\ \times \Im \left\{ D_{11}^{(e)} \left[B^2 \frac{k_z^2}{k^2} - \frac{k_z^2}{k^2} + 2B \frac{k_\perp k_z}{k^2} \right] \right. \\ + D_{22}^{(e)} A^2 + D_{33}^{(e)} \left[\frac{k_y^2}{k^2} + \frac{k_\perp^2}{k^2} B^2 - 2B \frac{k_\perp k_z}{k^2} \right] \\ + 2 D_{13}^{(e)} \left[B \frac{k_\perp}{k} \left(\frac{k_z^2}{k^2} - \frac{k_\perp^2}{k^2} \right) \right. \\ \left. \left. - \frac{k_\perp^2 k_z^2}{k^4} B^2 + \frac{k_\perp^2 k_z}{k^3} \right] \right\} dk\end{aligned} \tag{58}$$

where $[(\nu_e^p)_{AN}]_L$ is the well-known electrostatic (longitudinal) contribution to the anomalous electron momentum exchange rate

$$[(\nu_e^p)_{AN}]_L = -\frac{2}{u_{de} m_e n_e} \int \mathcal{E}_{k_\perp} k_\perp \Im \{\chi_e\} \, dk \tag{59}$$

and $\chi_e = D_{11}^{(e)}$ is the electrostatic susceptibility of the electrons. In the electrostatic limit ($\beta \to 0$) it can be verified that the integrand in Eq. (58) vanishes so that we are left with $(\nu_e^p)_{AN} \to [(\nu_e^p)_{AN}]_L$ and

$$\Im\{\chi_e\} = \Im\{D_{11}^{(e)}\} = \Im\{-D_{11}^{(i)}\} = \Im\{-\chi_i\}. \tag{60}$$

We shall demonstrate through the calculations of Section 3.7 that the transverse (electromagnetic) or finite-beta correction to $(\nu_e^p)_{AN}$ in Eq. (58) can be substantial, especially for a finite-beta plasma like that of the MPD thruster.

Equations (46) and (58) are equivalent but, for the present analytical discussion, we prefer, from here on to use the former (i.e. the electric field formalism)

because the resulting expressions are more compact. For our numerical calculations we shall apply the transformations in Eqs. (47) to Eq. (57) in order to obtain the $\boldsymbol{R}$ tensor from the $\boldsymbol{D}$ derived in our previous work [4] and quoted here in the appendix.

It is convenient to express $(\nu_e^p)_{AN}$ in units of a natural frequency. We choose, the lower hybrid frequency, ω_{lh}, because it is the natural plasma oscillation mode closest to the modes we are investigating, and normalize Eq. (46) to get

$$\frac{(\nu_e^p)_{AN}}{\omega_{lh}} = -\frac{v_{ti}}{u_{de}}\left(\frac{T_i}{T_e}\right)^{1/2}\frac{m_i}{m_e}\int\frac{\mathcal{E}_{k_\perp}}{n_0 T_i} \times \Im\left\{k_\perp r_{ce}\left[R_{zz}^{(e)}A^2 + R_{yy}^{(e)} + R_{zz}^{(e)}B^2 + 2R_{yz}^{(e)}B\right]\right\} d\boldsymbol{k}. \tag{61}$$

We have focused, above, on the anomalous electron momentum exchange rate. Similar derivations, with no conceptual difference, start from Eqs. (21) and (27) and lead to the following expressions for the ion and electron heating rates $(\nu_i^T)_{AN}$ and $(\nu_e^T)_{AN}$

$$\frac{(\nu_i^T)_{AN}}{\omega_{lh}} = \frac{4}{3}\int\frac{\mathcal{E}_{k_\perp}}{n_0 T_i}\Im\left\{\frac{\omega}{\omega_{lh}}\left[R_{zz}^{(i)}A^2 + R_{yy}^{(i)} + R_{zz}^{(i)}B^2 + 2R_{yz}^{(i)}B\right]\right\} d\boldsymbol{k} \tag{62}$$

$$\begin{aligned}\frac{(\nu_e^T)_{AN}}{\omega_{lh}} = \frac{4}{3}\frac{T_i}{T_e}\int\frac{\mathcal{E}_{k_\perp}}{n_0 T_i} &\times\Im\left\{\left[\frac{\omega}{\omega_{lh}} - k_\perp r_{ce}\left(\frac{T_i}{T_e}\right)^{1/2}\frac{u_{de}}{v_{ti}}\right]\right.\\ &\times\left[R_{zz}^{(e)}A^2 + R_{yz}^{(e)}B + R_{zz}^{(e)}B^2\right]\\ &+\frac{k_z}{k}\frac{u_{de}}{v_{ti}}k_\perp r_{ce}\left(\frac{T_i}{T_e}\right)^{1/2}\\ &\times\left[R_{zz}^{(e)}A + R_{xy}^{(e)} + R_{zz}^{(e)}B\right]\\ &+\frac{\omega}{\omega_{lh}}\left[R_{yy}^{(e)} + R_{yz}^{(e)}B\right]\\ &\left.-Ak_\perp r_{ce}\left(\frac{T_i}{T_e}\right)^{1/2}\frac{u_{de}}{v_{ti}}R_{xy}^{(e)}\right\}d\boldsymbol{k}.\end{aligned} \tag{63}$$

The above three equations are the sought expressions for our analysis of anomalous transport[5].

[5] *Winske et al.*[16] (1985) have derived expressions for the anomalous heating rates of ions and

3.5 Saturation Mechanisms

For the numerical analysis of anomalous transport in the MPD thruster plasma, the above three equations, along with the tensor elements in Eqs. (90)-(97), the linear dispersion relation

$$\det|R_{ij}(\omega,k)| = 0 \tag{64}$$

and the transformations in Eqs. (47)-(57) form an *almost* complete set of equations in terms of the following non-dimensional parameters:

$$\begin{aligned} & k r_{ce}, \quad \frac{\omega}{\omega_{lh}}, \quad \frac{\gamma}{\omega_{lh}}, \quad \frac{T_i}{T_e}, \quad \frac{u_{de}}{v_{ti}}, \\ & \Psi, \quad \beta_e, \quad \frac{\omega_{pe}}{\omega_{ce}}, \quad \frac{m_i}{m_e}, \quad \frac{\nu_e}{\omega_{lh}}. \end{aligned} \tag{65}$$

where $\omega_{lh} \simeq \sqrt{\omega_{ci}\omega_{ce}}$ is the lower hybrid frequency, β_e is the electron beta (ratio of electron thermal pressure to magnetic pressure), ω_{pe} is the electron plasma frequency and Ψ is related to the propagation angle θ (see Fig. (1)) scaled by the mass ratio

$$\Psi \equiv (m_e/m_i)^{1/2}\frac{k}{k_z} = \frac{(m_e/m_i)^{\frac{1}{2}}}{\cos\theta}. \tag{66}$$

The only lacking equation is one that relates the level of saturated microturbulence $\mathcal{E}_k/n_0T_i$ to the above parameters.

The formulation of this relation is, by far, the most formidable obstacle to the study of wave-particle transport, since such a relation must embody all the physics of the nonlinear saturation mechanism. The central question in this context concerns the mechanism through which the fluctuations, initiated by the instability, reach a steady-state. This mechanism dictates the magnitude and dependencies of the corresponding fluctuating energy density.

In this report we shall adopt and compare four different saturation mechanisms: ion trapping, electron trapping, ion resonance broadening and thermodynamic bound. The models for each of these mechanisms are discussed in more detail in Ref. [5, pp.128-135]. For our purposes here we only quote the resulting expression for each of these saturation models.

---

electrons in finite-beta plasmas. Their expressions differ from ours because of a difference in evaluating the ensemble-averages. In going from Eq. (37) to Eq. (38) above, for instance, these authors would neglect in the summation the cross-terms $\tilde{E}_l\tilde{E}_m$ with $l \neq m$ (see Equations (14) and (15) of that paper). There does not seem to be, however, a valid *a priori* reason to neglect such cross-terms[17]. Indeed, had we dropped these terms, the last term of the sum in the integrand of Eq. (46) would vanish. This term, $2R_{zz}^{(e)}B^2$, was found to be important for many situations we have investigated numerically. Furthermore, had we dropped the cross-terms it would not have been possible to recover the electrostatic contribution from Eq. (58) in the $\beta \to 0$ limit.

3.6 Thermodynamic Limit: The Fowler Bound

An upper limit for $\mathcal{E}_t$ was first derived by *Fowler*[18] (1968) from thermodynamic arguments,

$$(\mathcal{E}_t)_{FB} \leq \frac{1}{2} n_e m_e u_{de}^2, \tag{67}$$

and simply states that the energy in the turbulent fields cannot exceed the kinetic energy of the electron drift that is fueling the instability. For a convenient incorporation in our particular formulation, we recast the inequality above to read

$$\frac{(\mathcal{E}_t)_{FB}}{n_o T_i} \leq \frac{m_e}{m_i} \left(\frac{u_{de}}{v_{ti}} \right)^2. \tag{68}$$

3.6.1 Saturation by Ion Trapping

In situations where the excited wave spectrum is narrow due to the dominance of a single wave mode, a monochromatic wave saturation model, such as that behind particle trapping, can prove to be a viable mechanism for saturation. In such a case the saturation dynamics can be governed by the trapping of the particles in the potential wells of the growing mode thus limiting its growth. At saturation one can simply write

$$e\tilde{\phi} = \frac{1}{2} m_i \left(\frac{\omega_r}{k} \right)^2 \tag{69}$$

where ω_r/k is the phase velocity of the dominant mode and we have assumed that the ions are the particles being trapped. Again, we normalize the saturation model for compatibility with transport theory so that, using $e\tilde{\phi} \approx e\tilde{E}/k$ and $\mathcal{E}_k = \epsilon_0 |\tilde{E}_k|^2/2$, the above equation can be rewritten as

$$\frac{(\mathcal{E}_k)_{IT}}{n_o T_i} = \frac{1}{4 (k r_{ce})^2} \left(\frac{\omega_{ce}}{\omega_{pe}} \right)^2 \frac{T_e}{T_i} \left(\frac{\omega_r}{\omega_{lh}} \right)^4. \tag{70}$$

3.6.2 Saturation by Electron Trapping

Electron trapping is probably not a viable saturation mechanism for an instability in which electrons are collisional and are in broad-resonance with the unstable waves. We shall, however, include a model for electron trapping saturation in our calculations for the sake of reference. In analogy with ion trapping, we can write for the electrons as viewed from the ion rest frame

$$e\tilde{\phi} = \frac{1}{2} m_e \left(\frac{\omega_r}{k_z} - u_{de} \right)^2, \tag{71}$$

and after some algebraic manipulations,

$$\frac{(\mathcal{E}_k)_{ET}}{n_o T_i} = \frac{1}{4 (k r_{ce})^2} \left(\frac{\omega_{ce}}{\omega_{pe}} \right)^2 \frac{T_e}{T_i} \left[\Psi \frac{\omega_r}{\omega_{lh}} - k r_{ce} \frac{u_{de}}{v_{te}} \right]^4. \tag{72}$$

3.6.3 Saturation by Resonance Broadening

This mechanism relies on the broadening of wave-particle resonances by the random motion of particles in the turbulent electric field set-up by the microinstability.

If resonance broadening is to be important in our case, it would most probably rely on ion dynamics, since the electrons are already broadly resonant with the waves due to collisions and finite-beta effects while the ions are very narrowly-resonant[5].

Following *Gary* and *Sanderson*[19] who applied the *Dum-Dupree* resonance broadening formula[20] to the ions and found, after taking the velocity average $\int \Delta\omega f_{i_0}\, dv / \int f_{i_0}\, dv$,

$$(\mathcal{E}_k)_{IRB} = \frac{1}{2}\epsilon_0 B_0^2 \left(\frac{\omega_r}{k}\right)^2, \tag{73}$$

we specialize the ion resonance broadening model for our dimensionless parameters and obtain

$$\frac{(\mathcal{E}_k)_{IRB}}{n_0 T_i} = \frac{m_e/m_i}{(k r_{ce})^2} \frac{T_e}{T_i} \left(\frac{\omega_{ce}}{\omega_{pe}}\right)^2 \left(\frac{\omega_r}{\omega_{lh}}\right)^2. \tag{74}$$

3.7 Calculations of Anomalous Transport

Armed with the expressions for anomalous transport in Eqs. (61), (62) and (63) along with the tensor elements in Eqs. (90)-(97) (Appendix), the linear dispersion relation in Eq. (64), the transformations in Eqs. (47)-(57) and the saturation models in Eqs. (68), (70), (72), (74), we can now conduct a comparative numerical study of anomalous dissipation.

3.7.1 Classical Benchmarks

For benchmarks we shall use the following classical expressions for the momentum and energy exchange rates.

For the momentum exchange rate we take the classical Coulomb (electron-ion) collision frequency[9] for momentum relaxation $(\nu_e^p)_{CL}$

$$(\nu_e^p)_{CL} = \frac{n_e e^4 \ln\Lambda}{3(2\pi)^{3/2}\epsilon_0 m_e^{1/2} T_e^{3/2}} \tag{75}$$

where the plasma parameter Λ is given by

$$\Lambda = 9\left(\frac{4}{3}\right)\pi n_0 \lambda_{de}^3. \tag{76}$$

This collision frequency determines the classical Spitzer resistivity

$$(\eta)_{CL} = \frac{m_e (\nu_e^p)_{CL}}{n_0 e^2}. \tag{77}$$

For compatibility, we normalize with the lower hybrid frequency and cast the result in terms of our dimensionless parameters, to get

$$\frac{(\nu_e^p)_{CL}}{\omega_{lh}} = \frac{2}{\sqrt{2\pi}} \left(\frac{m_i}{m_e}\right)^{1/2} \frac{\omega_{pe}}{\omega_{ce}} \frac{\ln \Lambda}{\Lambda}. \tag{78}$$

For a heating rate benchmark we define a classical heating rate, $(\nu_e^T)_{CL}$, for Joule heating

$$(\nu_e^T)_{CL} \equiv \frac{1}{n_0 T_e} \frac{\partial}{\partial t} n_e T_e = \frac{2}{3} (\eta)_{CL} \frac{j^2}{n_0 T_e} \tag{79}$$

which yields

$$\begin{aligned} \frac{(\nu^T)_{CL}}{\omega_{lh}} &= \frac{8}{3\sqrt{2\pi}} \left(\frac{u_{de}}{v_{ti}}\right)^2 \frac{T_i}{T_e} \left(\frac{m_e}{m_i}\right)^{1/2} \frac{\omega_{pe}}{\omega_{ce}} \frac{\ln \Lambda}{\Lambda} \\ &= \frac{4}{3} \left(\frac{u_{de}}{v_{ti}}\right)^2 \frac{T_i}{T_e} \frac{m_e}{m_i} \frac{(\nu_e^p)_{CL}}{\omega_{lh}}. \end{aligned} \tag{80}$$

where the second equation shows the explicit dependence on the collision frequency.

Finally, we note that in calculating the anomalous rates we approximate the integrals, as commonly done in the literature, by the contribution of the dominant mode only (*i.e* for k^{**}), meaning that all the Fourier-decomposed properties are estimated at the doubly maximized growth (*i.e* maximized over wavelength and propagation angle)[6].

3.7.2 Numerical Results

Since β_e and u_{de}/v_{ti} are the two parameters that vary most within the plasma of the MPD thruster, they were chosen as the varying parameters of the calculations. When β_e is varied, u_{de}/v_{ti} is kept at 20, and when u_{de}/v_{ti} is varied, β_e is set at unity. The other parameters are $m_i/m_e = 73300$ (for argon), $T_i/T_e = 1$, $\nu_e/\omega_{lh} = 1$ and $\omega_{pe}/\omega_{ce} = 100$ for continuity with the calculations in of our previous studies[7].

[6]Although this simplification is followed by almost all anomalous transport calculations in the literature, (often without justification) one must, for quantitative accuracy, check to see whether, indeed, the k-resolved rate calculations vary weakly with the wavenumber in the region of parameter-space of interest. Although we have done a few cursory checks on the sensitivity of the rates to the details of the spectrum we have not evaluated the above calculation method over a comprehensive range to warrant its accuracy over the entire plasma parameter range of interest, since we are only concerned here with order-of-magnitude variations in the rates. More accurate calculations in the future should address this question.

[7]Higher collisional rates will be considered in the MPD thruster-specific calculations of the next section.

Effects of Plasma Beta The effects of plasma beta on the resistivity are shown in Fig. (2) where the ratio of anomalous to classical momentum exchange frequency (which is essentially the ratio of the corresponding resistivities (*cf* Eqs. (18) and Eq. (77)) is plotted versus beta for the parameters listed above. We immediately note that, even when plotted on such a compacted log-

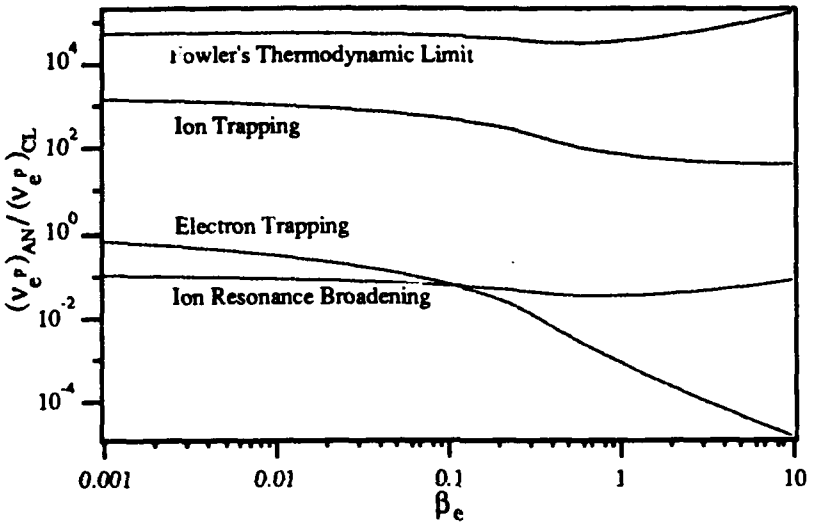

Figure 2: The anomalous momentum exchange frequency, $(\nu_e^p)_{AN}$, normalized by its classical counterpart and plotted versus the electron beta according to four saturation models. Argon with $u_{de}/v_{ti} = 20$, $T_i/T_e = 1$, $\nu_e/\omega_{lh} = 1$ and $\omega_{pe}/\omega_{ce} = 100$.

arithmic ordinate scale spanning eight orders of magnitude, all the curves can be seen to deviate from their $\beta_e \to 0$ asymptotes (which are practically reached at $\beta_e = .001$). These deviations are due to the electromagnetic corrections to the electrostatic limits, as separated in Eq. (58). We also note that the trapping models are most effected by finite-beta effects.

The ion trapping model is of special interest as discussed in Section 3.6.1 especially since it was the only one assumed in the purely electrostatic study of ref. [21]. We see that, when β_e is on the order of unity or greater, as is commonly the case of the MPD thruster plasma, the anomalous resistivity is an order of magnitude less than that predicted by the purely electrostatic limit.

The reason the anomalous resistivity decreases with increasing beta according to trapping models can be traced to the coupling with pseudo-whistler modes that we discussed in ref. [5]. As beta increases, the disturbances to the magnetic field do not have the time to dissipate (low Alfvén velocity) and significant

electromagnetic coupling arises. The unstable waves acquire some of the characteristics of oblique whistlers and consequently the most unstable modes shift to lower frequencies. Since the saturation level due to trapping scales with frequency to the fourth power (*cf* Eq. (70)), the end effect is a substantial reduction in the anomalous resistivity.

It is relevant, in the context of a comparative study, to mention that a plausibility argument based on the concept of minimum dissipation is usually invoked in the literature when saturation mechanisms are compared. According to this argument the mechanism requiring the least energy at saturation is favored. A comparative analysis based solely on this criterion can, however, be misleading if it does not consider the viability of the physical mechanism independent of the global thermodynamics.

We note from the plot that the Fowler bound on the calculated rates allows, in principle, for a wide latitude for anomalous resistivity to be important.

We should not expect the electron trapping model to dictate the transport for arguments already made in previous sections. Furthermore, we should mention that more careful studies of resonance broadening than was made at the time the mechanism was first proposed, have shown that its effects are limited to a redistribution of energy in k-space at low plasma beta, and that it does not result in enough dissipation to saturate an instability (such as the case of the lower hybrid gradient driven instability (LHGDI), for instance) . Therefore, for low β_e, ion trapping is the most viable mechanism. At these conditions, the anomalous resistivity can be quite dominant (as is observed in Fig. (2)), more than two orders of magnitude larger than the classical value, in agreement with the findings of ref. [21]. As beta increases, saturation by resonance broadening can become more viable especially since the turbulent saturation levels are considerably lower than those for ion trapping (as is clear from the same plot). Whether one or the other mechanism controls saturation depends, at least partly, on whether the spectrum is narrow or broad. Even though experimental data on turbulent fluctuations in the MPD thruster[10, 11] give evidence of a dominant narrow (peaked) spectrum of turbulence in the lower hybrid range, the considerably lower levels of saturation energy implied by the ion resonance broadening mechanism warrant its consideration as a contender in the control of turbulent transport. Of course, this question is best answered by computer particle simulations.

If ion resonance broadening does take over the control of saturation, anomalous transport can, for the parameters in the above calculations, be brought down below classical levels. One should therefore expect, by virtue of the substantial variability of the plasma beta within the MPD thruster plasma, that there are regions where anomalous resistivity dominates over its classical analog as there are regions where the converse is true. More on this issue will be said in Section 3.7.3.

The same comments we made above also apply for the anomalous electron heating rates that were normalized by the joule heating rate and plotted

in Fig. (3). It is clear from this plot that when ion trapping dominates, the

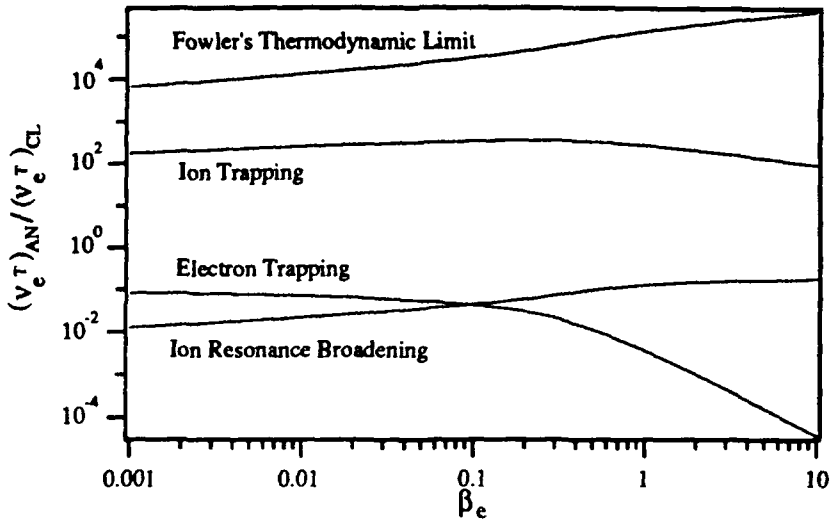

Figure 3: The anomalous electron heating rate, $(\nu_e^T)_{AN}$, normalized by the joule heating rate and plotted versus the electron beta according to four saturation models. Argon with $u_{de}/v_{ti} = 20$, $T_i/T_e = 1$, $\nu_e/\omega_{lh} = 1$ and $\omega_{pe}/\omega_{ce} = 100$.

anomalous heating rate is substantially larger than the electron joule heating rate. Ion heating rates are not shown here but were calculated in ref. [5] and were found to be similar in both magnitude and dependence as their electron counterparts.

To compare the two rates we have calculated their ratio and plotted the result in Fig. (4). There is only one curve in this figure because the various saturation models cancel out in the division. Since this ratio is independent of the saturation details, it is more accurate than the other quantities we have calculated. We note from this figure that, in the electrostatic limit, the two anomalous heating rates are basically equal. This feature is in contrast to the way electrons and ions are heated classically (especially for a heavy atom like argon) and is a well-known characteristic of the electrostatic LHCDI (or the modified two-stream instability, MTSI) as noted in ref. [22, 23]. Since the ions, are heated by the instability-induced turbulence at rates comparable to those of the electrons, and since in the MPD thruster, the electron energy is strongly tied to excitation and ionization through inelastic collisions, anomalous heating can offer an answer to the long standing question of why the ion temperature is somewhat higher than the electron temperature. Of course, for this argument to be true not only $(\nu_e^T)_{AN}$ must be comparable to $(\nu_i^T)_{AN}$, but the saturation

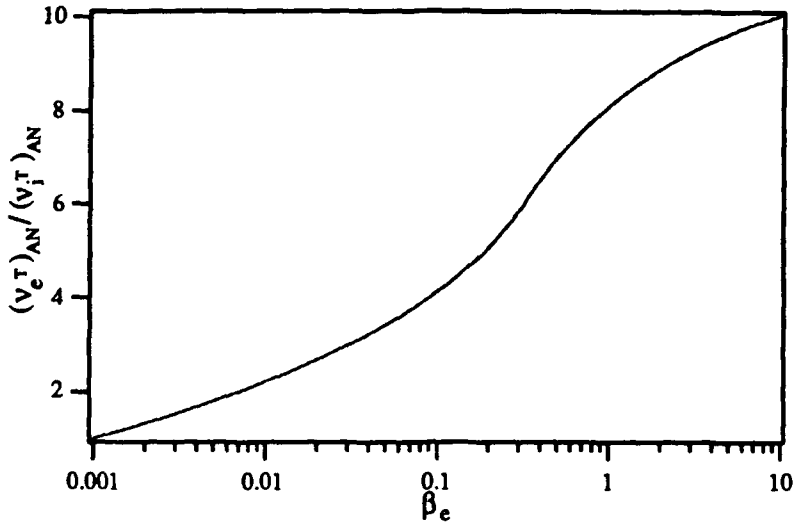

Figure 4: The anomalous electron heating rate, $(\nu_e^T)_{AN}$, normalized by the anomalous ion heating rate, $(\nu_i^T)_{AN}$, plotted versus the electron beta. Argon with $u_{de}/v_{ti} = 20$, $T_i/T_e = 1$, $\nu_e/\omega_{lh} = 1$ and $\omega_{pe}/\omega_{ce} = 100$.

level must be high enough to warrant the dominance of anomalous heating over classical heating. Such is the case when the instability saturates by trapping ions.

The above argument about the relative temperatures is strongest in the electrostatic limit and is in agreement with ref. [21]. When electromagnetic effects start to become important with increasing beta, the same figure shows a degradation of the heating parity towards a progressively preferential heating of electrons. This finding is in agreement with that of ref. [16] where only the collisionless limit was studied. This degradation in heating parity is not strong enough, however, to weaken the grounds for the above argument concerning the relative temperatures, especially for a heavy atom like argon. Indeed, we see from the same figure that a four-octave increase in beta does not change the order of magnitude of the relative heating ratio.

The increase of preferential electron heating with increasing beta may be partly due to the fact that, at low beta, the instability has its dominant modes oriented at small angles to the magnetic field ($k_z/k \simeq (m_e/m_i)^{1/2}$ or $\Psi \simeq 1$) as was found in our previous studies[3], and consequently "perceives" the electron with an effective mass comparable to that of the ions[22]. As beta increases, electromagnetic coupling with oblique pseudo-whistlers cause the dominant modes to propagate more obliquely, as first noted by refs. [24] and [25] and extended

by us, in ref. [5], to the collisional domain. Consequently, the effective electron mass decreases and the electrons become much easier to heat than the ions.

Effects of the Drift Velocity The effects of the drift velocity are illustrated in the plots of Figs. (5) and (6) for the same parameters as above but with β_e set to unity and u_{de}/v_{ti} varying between 10 and 100.

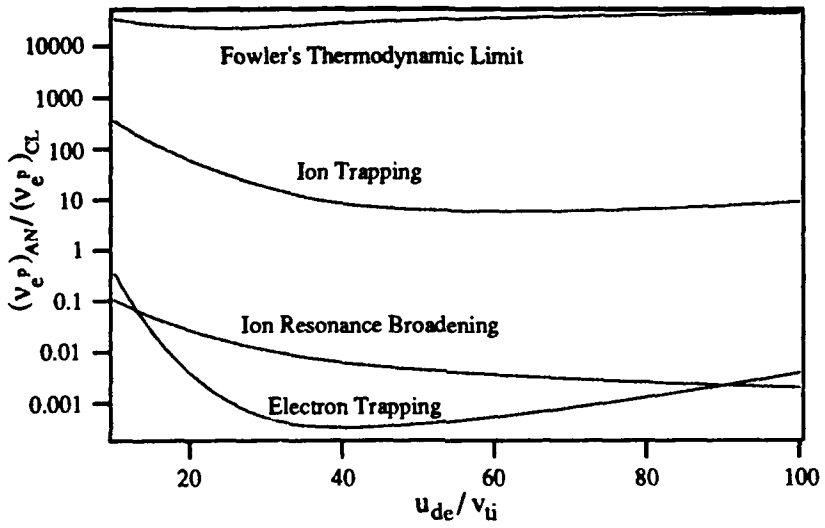

Figure 5: The anomalous momentum exchange frequency, $(\nu_e^p)_{AN}$, normalized by its classical counterpart and plotted versus the normalized drift velocity according to four saturation models. Argon with $\beta_e = 1$, $T_i/T_e = 1$, $\nu_e/\omega_{lh} = 1$ and $\omega_{pe}/\omega_{ce} = 100$.

In reference to Fig. (5) we note that the general decreasing trend of anomalous resistivity with the drift velocity, once the instability is onset[8], is not intuitive. One would expect that an increase in the free energy source of the instability would enhance the anomalous resistivity effect. In ref. [21] the same trend was found but no explanation was given.

This trend can be understood once we realize that the scaling of the linear growth rate of the dominant mode (which does increase with the drift velocity) does not *necessarily* reflect in weak turbulence (quasi-linear) transport scaling since the dependencies of the saturation mechanism (which is extraneous to linear theory) can overwhelm linear trends. This becomes clearer by noting that although an increase in the drift velocity does enhance the linear growth rate

[8]The u_{de}/v_{ti} thresholds for the onset of the instability (start of positive linear growth) are not marked on these plots because they are on the order of unity.

of the dominant mode as found in a previous study of ours[3], it also shifts the modes to more oblique propagation and lowers their frequencies. Even though the instability goes to longer wavelength[5], the dependence of the saturation level for a trapping mechanism (*cf* Eq. (70)) scales with the frequency to the fourth power so that the frequency scaling of the saturation mechanism overpowers the growth scaling of the linear modes[9].

The Fowler bound, on the other hand, whose scaling is more strongly tied to the free energy source, does increase monotonically with the drift velocity, as seen from the resistivity plot.

As expected from the above beta-dependence study, anomalous electron heating rates exceed those of the ions for the present case of $\beta_e = 1$. The preferential electron heating is further enhanced by increasing drift velocity as can be seen in Fig. (6). The reason for this behavior is similar to the one given

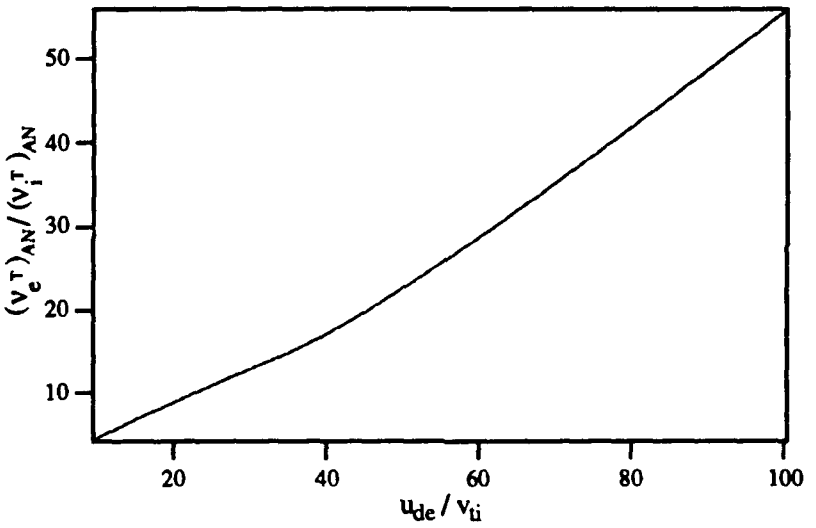

Figure 6: The anomalous electron heating rate, $(\nu_e^T)_{AN}$, normalized by the anomalous ion heating rate, and plotted for the same conditions as in Fig. (5).

above in the context of electromagnetic enhancement of electron preferential heating. This is so because both increasing beta and increasing drift velocity act to shift the instability toward more oblique propagation thus reducing the

[9]This trend is further accentuated for saturation by electron trapping because, in addition to the above arguments, the saturation level scales with Ψ^4 and Ψ decreases considerably (oblique propagation) with increasing drift velocity. At very high drift, the Doppler shift term in the saturation model (*cf* Eq. (72)) becomes more significant and reverts the trend, which explains the rise of the electron trapping curve in Fig. (5) at high values of u_{de}/v_{ti}.

large $\bar{m}_e$-effect (where $\bar{m}_e$ is the effective electron mass that scales with the square of ψ) and subjecting the now "lighter" electrons to more heating.

3.7.3 MPD Thruster Calculations

We have, in the above calculations, chosen a set of parameters that is generally representative of the MPD thruster plasma. There is, however, one exception. It is the value of ν_e/ω_{lh} which we have set equal to unity as a compromise between having to represent a collisional plasma and providing a link with previous studies. Moreover, many of the complex interactions between the natural plasma modes, the free energy source and collisions are most pronounced when the collision frequency is on the order of the oscillating frequency. We now, supplement our calculations with results obtained at collisional levels more appropriate of the MPD thruster plasma.

In order to approximate a typical range for MPD thruster plasma collisionality, we consider the typical range for the variation of temperature and density. For more detail on how the various parameters of interest vary within the MPD thruster discharge the reader is referred to the recent parameter review in ref. [10]. Assuming that T_e varies between 1.5 and 3 eV, while n_0 ranges between 10^{20} and 1.5×10^{22} m^{-3}, we can calculate a lower and upper bound for ν_e/ω_{lh} in argon from Eq. (78) to be 25 and 500, respectively, where we have fixed ω_{pe}/ω_{ce} at 100 for compatibility with the above calculations.

For the results shown in Fig. (7) we have chosen to fix beta at unity to preserve electromagnetic effects and varied u_{de}/v_{ti} from 100 down to the threshold of the instability, which, although slightly exaggerated in the figure, was at $u_{de}/v_{ti} \simeq 1.5$. For each of the three considered mechanisms the plot shows a band whose upper line corresponds to the moderately collisional condition $\nu_e/\omega_{lh} = 25$ ($T_e = 3$ eV, $n_0 = 10^{20}$ m^{-3}) and whose lower (broken) line corresponds to the strongly collisional condition $\nu_e/\omega_{lh} = 500$ ($T_e = 1.5$ eV, $n_0 = 1.5 \times 10^{22}$ m^{-3}).

The trends in this plot are similar to those already illustrated in Fig. (5) which indicated that we have not jeopardized any physics by assuming $\nu_e/\omega_{lh} = 1$ previously.

We note from the figure that, although the Fowler bound allows for a large microturbulent contribution to the resistivity, ion resonance broadening might cause the instability to saturate at low levels. Even though arguments have been advanced recently discounting the effectivity of such a mechanism, it should not be totally discounted pending strong evidence from computer particle simulations and/or dedicated experiments.

We furthermore see that, in the case of ion trapping saturation, once the instability is onset, the importance of anomalous resistivity in the MPD thruster plasma is not as much dictated by the drift velocity (since the two limiting curves are quite flat), as one would intuitively suspect, as it is dictated by the level of collisionality. Indeed, if collisionality is strong, anomalous resistivity can be kept below classical levels even if the instability is excited and even if ion trapping

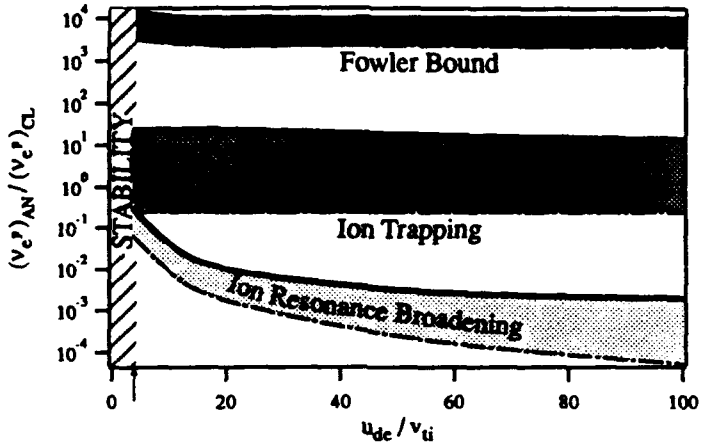

Figure 7: The anomalous momentum exchange frequency, $(\nu_e^p)_{AN}$, normalized by its classical counterpart and plotted versus the normalized electron drift velocity according to three saturation models. The upper line of each band corresponds to the moderately collisional condition $\nu_e/\omega_{lh} = 25$ ($T_e = 3$ eV, $n_0 = 10^{20}$ m^{-3}) and the lower (broken) line corresponds to the strongly collisional condition $\nu_e/\omega_{lh} = 500$ ($T_e = 1.5$ eV, $n_0 = 1.5 \times 10^{22}$ m^{-3}). Argon with $\beta_e = 1$, $T_i/T_e = 1$, and $\omega_{pe}/\omega_{ce} = 100$.

is responsible for saturation, as is clear from the plot[10]. This implies that low density regions of the MPD thruster discharge, such as regions depleted from charge due to the $j_z B_\theta$ Lorentz force component, tend to be more vulnerable to anomalous resistivity than denser (or more collisionally dominated) regions. This trend is in agreement with the well-known fact that dissipation in charged-depleted regions of the device, like the anode vicinity[26], is enhanced by weak collisionality.

Stated differently, under MPD thruster plasma conditions and for the microinstabilities in question, the level of anomalous contribution to resistivity is dictated to a large extent by the parameter ν_e/ω_{lh}. It is interesting to note that this parameter is directly related to the electron Hall parameter Ω_{H_e}. Indeed, it is just the inverse of the electron Hall parameter scaled by the square root of the mass ratio

$$\Omega_{H_e} \equiv \frac{\omega_{ce}}{\nu_e} = \frac{(m_i/m_e)^{1/2}}{\nu_e/\omega_{lh}}. \tag{81}$$

[10]It must be said, however, that even in the case of high collisionality ($\nu_e/\omega_{lh} \simeq 500$) where anomalous resistivity is kept below classical levels, it is still a finite fraction of its classical counterpart (about 25% in the above calculations), as can be seen from the same plot (again, assuming ion trapping saturation).

The known scaling of the anode voltage drop with the Hall parameter (see for instance the recent measurements in ref. [26]) that constitutes one of the most dissipative sinks for the low-power MPD thruster is thus another invariant behavioral trait of the accelerator that could possibly be explained by the effects of microinstabilities.

The anomalous ion and electron heating rates were also calculated in ref. [5] and found to have the same general trends as those of the anomalous resistivity.

We now have all that we need to cast the anomalous transport models in a form that can be used in plasma fluid codes. This will be documented in th enext sections.

4 Anomalous Transport Models and their Inclusion in Fluid Codes

4.1 Goals

A spatial resolution of the realms of anomalous and classical transport within the MPD thruster discharge and their dependence on the accelerator's operating conditions can only be addressed accurately with an improved fluid code that incorporates the above theories in a self-consistent fluid-kinetic description. This may be accomplished by carrying *a priori* calculations of the relevant anomalous transport for the expected parameter-space covered by typical numerical simulations then fitting the calculations with polynomial expressions. These expressions become the transport models suitable for inclusion in codes for the self-consistent numerical simulation of MPD thruster flows.

4.2 Final Models

In general the microstability (and hence microturbulence) description, detailed in the sections above, depends on the following set of eight independent macroscopic parameters

$$kr_{ce}, \quad \Psi, \quad \frac{m_i}{m_e}, \quad \frac{\omega_{pe}}{\omega_{ce}}, \quad \beta_e, \quad \frac{u_{de}}{v_{te}}, \quad \frac{T_i}{T_e}, \quad \Omega_{H_e} \tag{82}$$

The first two parameters kr_{ce} (r_{ce} being the electron cyclotron radius) and Ψ represent the normalized wavenumber and propagation angle (with respect to the magnetic field) of the oscillations respectively and are varied to growth-maximize the solutions. Since all anomalous transport rates used here were calculated at maximum growth these two parameters drop out of the final models. The mass ratio m_i/m_e is that of argon. All solutions were found in the calculations of the previous sections to be very insensitive to the fourth parameter, namely the ratio of electron plasma frequency to the electron cyclotron frequency ω_{pe}/ω_{ce}, as long as that ratio exceeded 10 which was the case for the

simulations conducted so far[27, 28]. Similarly, the solutions were weakly dependent on β_e (the ratio of electron thermal pressure to magnetic pressure) as long as the electron Hall parameter did not exceed 10. Although that was the case for the numerical simulations in Refs. [27, 28], it is expected that the simulation of more realistic geometries at high total currents would raise the electron Hall parameter enough to require the full inclusion of finite-beta effects.

The last three parameters are the most important for our problem. First, u_{de}/v_{ti} must reach a threshold for the instability to be excited and hence for anomalous transport to be operative. For the entire region of the investigated parameter-space that threshold was very near 1.5. Second, the ion to electron temperature ratio plays a role in scaling the level of turbulence. Invariably for our parameter-space, it was found that increasing T_i/T_e causes a devaluation of anomalous transport. The most important of all the macroscopic parameters turned out to be the last one namely the electron Hall parameter Ω_{H_e}.

The anomalous resistivity η_{AN}

$$\eta_{AN} \equiv \frac{m_e(\nu_e)_{AN}}{e^2 n_e}, \tag{83}$$

calculated using the theory presented in the above sections, and normalized by its classic counterpart $\eta_{Cl} \equiv m_e\nu_e/e^2n_e$ is shown in Fig. (8). It is important to note that an increase in the electron Hall parameter for typical values of T_i/T_e leads to a very significant increase in the anomalous resistivity *if* the parameter u_{de}/v_{ti} is above the stability threshold. It is interesting to note that the scaling of this ratio with the Hall parameter is in general agreement with that recently inferred by Gallimore[29] from measurements in the anode region.

A similar plot is shown in Fig. (9) for the ion heating rate $(\nu_i^T)_{AN}$ normalized by the Coulomb frequency.

A two-parameter, variable cross-term, least square fit was made to the calculated rates shown in Figs. (8) and (9) in order to make them suitable for inclusion in plasma fluid flow codes.

The resulting two-parameter interpolating polynomial for $(\nu_i^T)_{AN}/\nu_{ei}$ has an average accuracy of 15% and reads

$$\begin{aligned}\frac{(\nu_i^T)_{AN}}{\nu_{ei}} \;=\; & 5.36\times10^{-5} + 1.29\times10^{-5}\,\Omega \\ & + 6.03\times10^{-6}\,\Omega^2 + 9.44\times10^{-8}\,\Omega^3 \\ & + \frac{T_h}{T_e}(-7.55\times10^{-7} - 5.41\times10^{-6}\,\Omega \\ & - 3.93\times10^{-6}\,\Omega^2).\end{aligned} \tag{84}$$

The ions are heated by the turbulent fluctuations at a rate $(Q_i)_{AN} = \frac{3}{2}(\nu_i^T)_{AN}T_h$

The effective conductivity introducing the anomalous resistivity effect to the

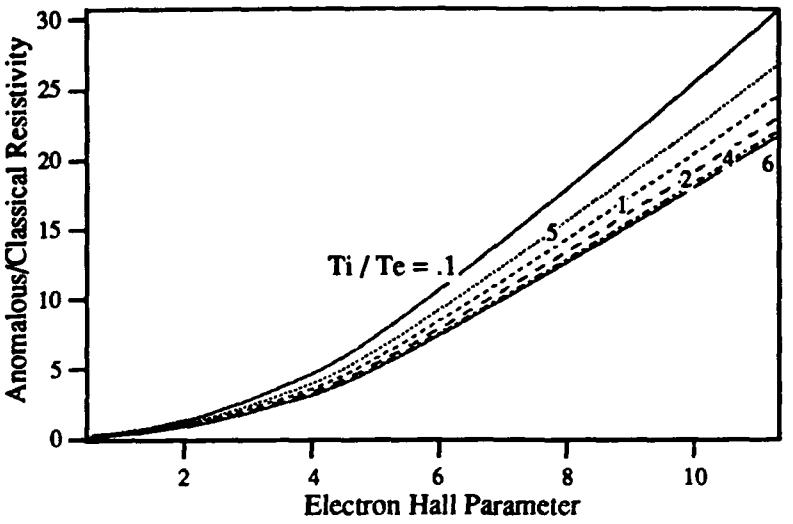

Figure 8: Ratio of anomalous resistivity to classical resistivity as a function of the electron Hall parameter and T_i/T_e with u_{de}/v_{ti} exceeding 1.5,

flow code has the form

$$\sigma_{eff} = \frac{e^2 n_e}{m_e(\nu_{ei} + (\nu_e^P)_{AN})}, \tag{85}$$

where $(\nu_e^P)_{AN}$ is the electron-wave momentum exchange frequency, which is again computed through an interpolating polynomial of average accuracy of 10%

$$\begin{aligned} \frac{(\nu_e^P)_{AN}}{\nu_{ei}} &= 0.192 + 3.33 \times 10^{-2}\ \Omega + .212\Omega^2 \\ &\quad - 8.27 \times 10^{-5}\ \Omega^3 + \frac{T_h}{T_e}(1.23 \times 10^{-3} \\ &\quad - 1.58 \times 10^{-2}\ \Omega \\ &\quad - 7.89 \times 10^{-3}\ \Omega^2). \end{aligned} \tag{86}$$

The use of these models in fluid code may proceed in the following way. At all the gridpoints where $u_{de}/v_{ti} < 1.5$ both, $(\nu_e^P)_{AN}$ and $(\nu_i^T)_{AN}$ are set to zero and all transport is assumed purely classical. Otherwise, the anomalous rates are computed from the above polynomials using the instantaneous macroscopic parameters and folded back into the flow equations at every time step thus insuring self-consistency.

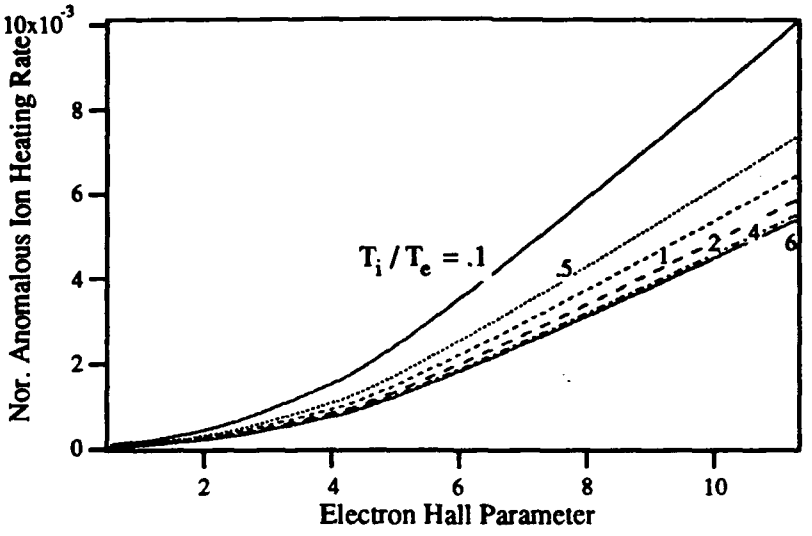

Figure 9: Anomalous ion heating rate normalized by the Coulomb frequency as a function of the electron Hall and T_i/T_e with u_{de}/v_{ti} exceeding 1.5

4.3 Fluid Code Description

The plasma fluid code used to test the anomalous transport models derived above was developed at our laboratory partly under the AFOSR grant. It is described in more detail in refs. [27, 28]. We provide here a brief description of the code. Our focus will instead be on the calculations made with that code under the support of AFOSR.

The results presented in this final report are for a cylindrical MPD thruster-geometry. The present code, however, can handle any axi-symmetric geometry.

The flow field code uses a finite-volume discretization with artificial dissipation described by Jameson[30]. The time stepping is done via the explicit Euler Forward method, and convergence is accelerated using a multigrid iteration first proposed by Jameson and Jayram[31]. These methods yield a second order steady-state solution to the conservation equations.

The solution of the conservation equations through the finite volumes/Euler forward routine is alternated with the solution of the electromagnetic equation, until consistency among all the parameters is achieved.

The stream function equation is solved with a second-order nonlinear explicit scheme developed at EPPDyL. After a central difference discretization is

performed, the stream function equation assumes the form

$$\zeta_1 \psi_{ij} + \zeta_2 = 0. \tag{87}$$

Here ψ_{ij} stands for the value of ψ at the i^{th} horizontal and j^{th} vertical discrete steps. The coefficients ζ_1 and ζ_2, then, are functions of the differential equation's coefficients and of $\psi_{i-1,j}$, $\psi_{i+1,j}$, $\psi_{i,j-1}$, $\psi_{i,j+1}$ Each iteration step we set

$$(\psi_{ij})^{(n+1)} = -\left(\frac{\zeta_2}{\zeta_1}\right)^{(n)}, \tag{88}$$

until $(\psi_{ij})^{(n+1)}/(\psi_{ij})^{(n)}$ is equal to 1. Using as initial guess the value of ψ computed at the previous MacCormack step, convergence is achieved in a number of steps ranging between 1 and 250.

These methods represent an improvement with respect to the MacCormack method used previously since it decreases running time by up to a factor of eight while reducing the steady-state residual. The model was coded in APL2 (taking full advantage of the inherent vectorizing capability of the language) and has been run on a variety of machines ranging from a Mac Quadra (1.2 Mflops) to an IBM ES/3090 600J Supercomputer where specialized APL2 compilers can allow convergence to be reached in less than 30 minutes of CPU time.

4.4 Results

This section will first discuss the performance curves obtained running at various current levels, with and without anomalous transport, and compare them to experimental data taken by Burton for a FSBT[32]. Two high current runs (18 kA), one with classical and one with anomalous dissipation, will then be compared, in order to asses in what areas of the thruster anomalous transport has the greatest impact. Furthermore, current distribution patterns will be compared with measured ones. The current density distribution for simulations with and without anomalous transport will also be shown, together with an experimental distribution obtained by Gilland[33].

Henceforth, the runs in which the conservation equations include anomalous transport coefficients will be denoted as "anomalous", whereas those not containing anomalous transport will be called "classical runs".

4.4.1 Discussion of Performance Curves

The code was run with a mass flow rate of 6 g/s and with currents ranging from 7 kA to 18 kA. The code diverged for higher currents. Runs were made both with and without anomalous transport dissipation terms present in the calculation. Plots of thrust, voltage and efficiency versus $J^2/\dot{m}$ are shown for these runs along with experimental data when appropriate.

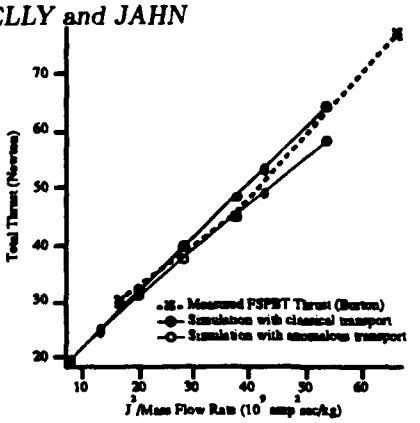

Figure 10: Calculated thrust from simulations with and without anomalous transport compared with measured FSBT thrust measured by Gilland[33] and Burton[32].

As is evident from Fig. (10), thrust scales as the square of the current individually for the case with and without anomalous transport. Both classical and anomalous predictions compare very well with the measured Benchmark values, which in turn are very close to the theoretical Maecker thrust[34] for the higher range of specific impulse ($J^2/\dot{m} \geq 40$ kA^2 sec/g). At lower values of $J^2/\dot{m}$, the measured thrust data exceed the Maecker law prediction. The simulations, however, were able to account for that excess as can be seen from the figure. It is also important to note that the thrust from the anomalous run becomes appreciably lower as $J^2/\dot{m}$ increases. This may be attributed to the fact that for higher T_h (anomalous case), the gas pressure decreases less along the chamber, so that the $-\nabla p_h$ force term is reduced.

Figure (11) shows the calculated voltage drop across the plasma (from the anode to the cathode). The calculated voltages do not include electrode sheath falls and therefore cannot be easily compared to the measured terminal voltage of the thruster. The voltage starts being consistently higher in the anomalous case only for the higher currents (above around 40 kA^2 sec/g).

The increase in the voltage and the decrease in thrust, due to anomalous transport, translate directly into a degradation in the thrust efficiency. To see the extent of this degradation, the thrust efficiency is calculated through the formula

$$\eta = \frac{F^2}{2\dot{m}JV}. \tag{89}$$

In Fig. (12) the efficiency is plotted, again, versus $J^2/\dot{m}$. While for currents below 10 kA ($J^2/\dot{m} \leq 20$ kA^2 sec/g) there is hardly any difference between the classical and the anomalous cases, for higher currents the efficiency is substantially lower with anomalous transport dropping by 13% at $J^2/\dot{m} = 55$ kA^2 sec/g. Furthermore, efficiency from anomalous runs tends to reach a plateau around

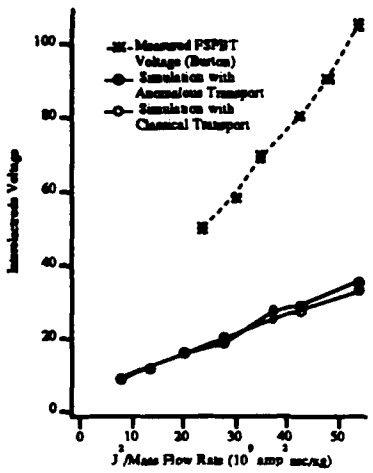

Figure 11: Plasma fall for simulations with and without anomalous transport. The calculated voltage does not include electrode sheath falls.

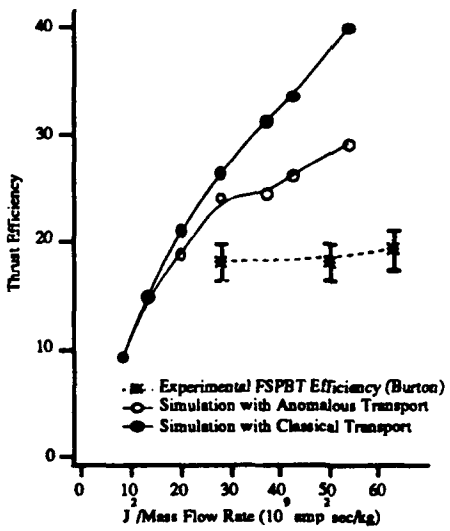

Figure 12: Thrust efficiency for simulations with and without anomalous transport compared with measured FSBT values.

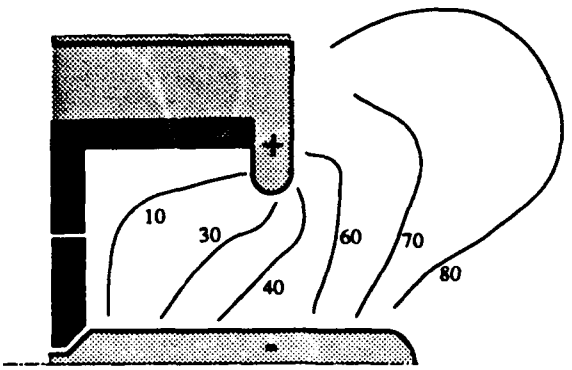

Figure 13: Current contour lines, in percentage of enclosed total current, as measured by Gilland[33]. ($J^2/\dot{m} = 30$ kA^2 sec/g).

25% for $J^2/\dot{m} \geq 30$ kA^2 sec/g, while in the classical transport case it keeps increasing. The shape of the efficiency curve for the anomalous runs, then, is closer to the plateau shape of the experimental curve. Even the lower efficiencies predicted by the simulation with anomalous transport are higher than the experimentally measured values. This discrepancy is due to a large extent to the fact that this numerical simulation does not include the voltage drops from the electrode sheaths. If the experimental total voltage were reduced by the sheath voltage, the numerical and experimental curves would approach each other significantly. Gallimore[29], in fact, has shown that the anode fall voltage increases monotonically with $J^2/\dot{m}$, and reaches values as high as 40 volts around $J^2/\dot{m} = 50$ kA^2 sec/g. Greater accuracy may be expected with the use of a more accurate geometric thruster configuration (with a varying cross-section) through the introduction of a transformation of coordinates in the model's equations. This will be the next step in our future studies. Furthermore, the extent to which viscous effects may help approaching the experimental values will also be explored in future investigations.

4.4.2 Current Distribution

Current distribution in a full-scale Princeton Benchmark Thruster for $J^2/\dot{m} = 30$ kA^2 sec/g is shown in Fig. (13) as measured by Gilland[33]. Current distribution as predicted by the anomalous transport numerical simulation is also shown (Fig. (14)).

It can be noted from these two figures that, along the cathode, which is the region where the geometric configurations are most similar, the calculated current distribution is evenly spread as in the experiments, with attachment going

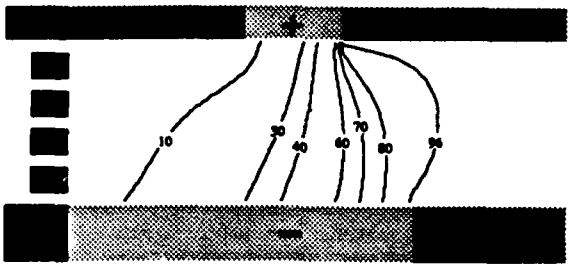

Figure 14: Current contour lines, in percentage of enclosed total current, as predicted by a flow model with anomalous transport. ($J^2/\dot{m} = 30$ kA^2 sec/g).

all the way to the root. Furthermore, the current pattern *inside* the discharge chamber is well predicted both in shape (contour lines curvature and inclination) and magnitude. This is the case up to the 60% line downstream of which the calculated current does not "balloon" out as much as in the experiments undoubtedly because of the presence of the downstream insulators imposed on the modeled geometry. Particularly, the insulator downstream of the anode does not allow attachment to the anode front like in the experiments.

4.4.3 Comparison Between a Classical and an Anomalous Run for High Current

We will now present two runs, one with classical and one with anomalous transport, at a current level of 18 kA and a mass flow rate of 6 g/s, and discuss the most striking differences between the two. In particular, resistivity and plasma heating will be shown to be significantly enhanced by plasma microturbulence.

Of course, changing the conductivity as a result of anomalous effects may affect the current attachment on the electrodes. Figures (15) and (16) show the distribution of current for the classical and for the anomalous runs. Since the conductivity is higher in the plume, for the classical case the current is blown more downstream. Furthermore, there is greater attachment at the tip of the anode for the classical run, again because of the higher relative conductivity there as will become apparent from the resistivity plot shown further below.

As mentioned above, anomalous transport is possible only in regions where u_{de}/v_{ti} exceeds 1.5. Moreover, once anomalous transport effects are onset in a certain region, their magnitude increases monotonically with the electron Hall parameter as can be seen from Eqs. (8) and (9). Figure (17) shows a map of the electron Hall parameter, Ω_e, in locations at which anomalous transport arises (i.e. regions with $u_{de}/v_{ti} \geq 1.5$). For such high a current as 18 kA, and unlike the case investigated in our last study[27], anomalous transport can be expected

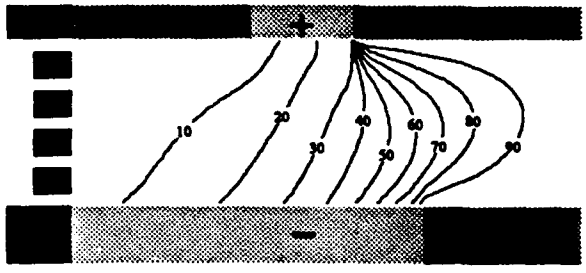

Figure 15: Enclosed current lines for the simulation with classical transport ($J = 18$ kA, $\dot{m} = 6$ g/s). The number along each line indicates what percentage of the total current is upstream of the line.

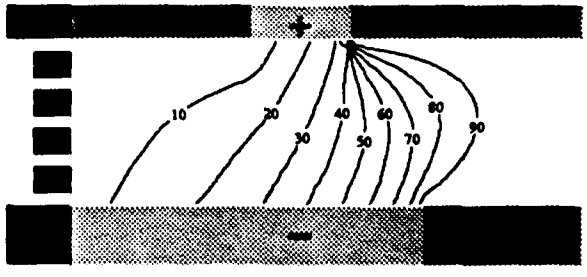

Figure 16: Enclosed current lines for the simulation with anomalous transport ($J = 18$ kA, $\dot{m} = 6$ g/s).

to affect a substantial portion of the discharge. The plot in Fig. (17) directly allows the identification of critical regions of the discharge from the point of view of anomalous transport. It is evident that the cathode root and tip and the anode tip are most critical.

The criticality of these regions is further supported by the resistivity map of Fig. (18) where the ratio of "anomalous" to "classical" resistivities (i.e. using the resistivities calculated from the anomalous and classical runs) is shown. The pronounced anomalous resistivity enhancement in the immediate vicinity of the anode tip is very reminiscent of the enhanced resistivities inferred by Gallimore[29] from local measurements near the anode. This further substantiates our earlier speculations[5, 27] that a substantial part of the infamous "anode drop" may be related to the turbulent effects induced by microinstabilities.

An appreciation of the extent and regional preference of anomalous plasma heating can be obtained by comparing the maps of Fig. (19) and Fig. (20). The two maps are of the ion temperature from the classical and anomalous runs respectively. It is clear from these figures that anomalous transport can cause enhanced plasma heating in specific regions. The "hot spot" near the backplate at the cathode root has been observed in our previous study[27] and has been suspected to play a role in backplate erosion. Backplate erosion is the only erosion mechanism that has been shown experimentally[35, 36] to occur along with the appearance of "instabilities" in the terminal voltage of the thruster. It can be noted from Fig. (19) that in the absence of microinstabilities this "hot-spot" disappears. The presence of such a spot has not been established experimentally yet and could provide a check on the predictive ability of the model.

Finally, we show in Fig. (21) (T_i/T_e from the classical run) and Fig. (22) (T_i/T_e from the anomalous run) that microturbulence may be at least partly responsible for the fact that T_i/T_e can exceed unity in the MPD thruster as is well known from experiments. This ratio never exceeded unity in our classical runs.

We have demonstrated that performance predictions from models with microturbulent transport compare more favorably with experiments than do predictions from models without such anomalous effects. Furthermore, the distribution of current, resistivity and heavy species temperature within the thrust chamber shows heat dissipation patterns which may explain some features of MPD thruster operation such as the anode drop and backplate erosion.

Among the improvements that can be applied to the numerical model presented above are an accurate representation of viscosity and non-equilibrium rate kinetics and most urgently, in light of the recent measurements in ref. [37] (that confirmed earlier speculations of anomalous ionization) more realistic ionization models including microturbulent effects.

5 Conclusions

We have addressed in detail the problem of anomalous transport in the MPD thruster and showed through numerical simulation how the inclusion of turbulent effects in fluid codes can improve the predictability and realism of fluid codes. We discussed the theoretical background and derivations for the transport models, and reduced our models to the form of polynomials. We included these polynmials in an advanced fluid code and studied various features of the flow that are impacted by the effects of plasma turbulence.

Now that the models have been derived and tested we have proceeded to the dissemination of the results to other workers in the field. Since we have cast our bottom-line results in the form of simple polynomials that depend only on macroscopic properties, they are thus ready for inclusion in *any* two-fluid code which could then be used for more realistic calculations of MPD thrusters including the effects of plasma turbulence caused by the existence of instabilities.

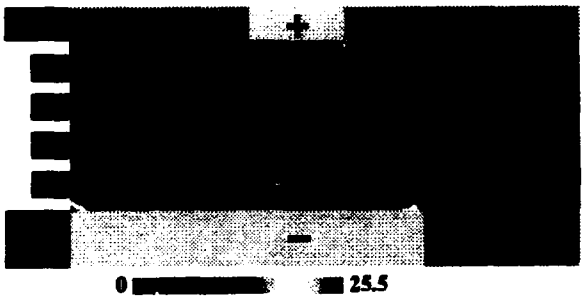

Figure 17: Electron Hall parameter in regions where anomalous transport is active ($u_{de}/v_{ti} \geq 1.5$). Critical regions are those with higher values of the Hall parameter.

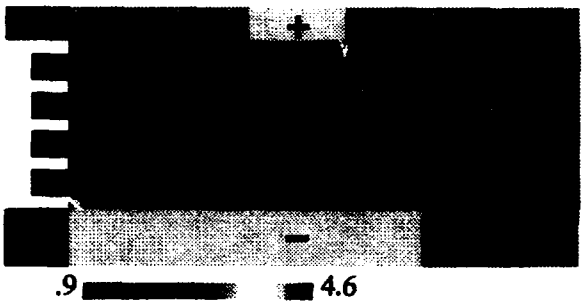

Figure 18: Ratio of "anomalous" to "classical" resistivities (i.e. using the resistivities calculated from the anomalous and classical runs). (J = 18 kA, $\dot{m}$ = 6 g/s).

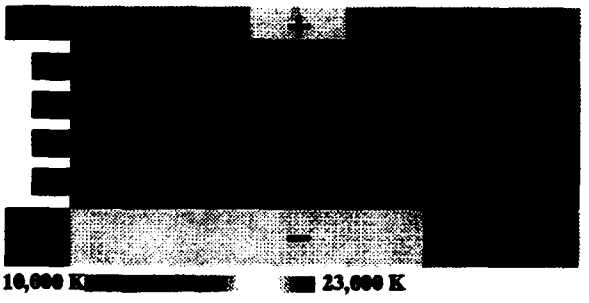

Figure 19: Heavy species temperature for the simulation with classical transport (J = 18 kA, $\dot{m}$ = 6 g/s).

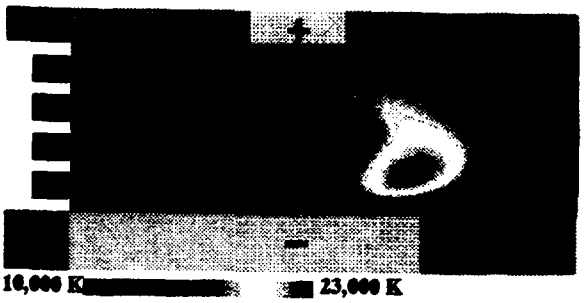

Figure 20: Heavy species temperature for the simulation with anomalous transport showing regions with enhanced ion heating due to microturbulence. ($J = 18$ kA, $\dot{m} = 6$ g/s).

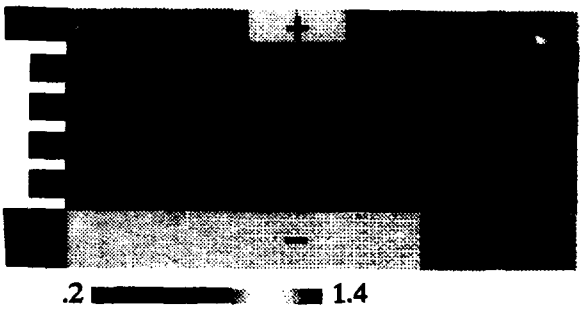

Figure 21: Ratio of ion to electron temperatures for the simulation with classical transport (($J = 18$ kA, $\dot{m} = 6$ g/s)). Note that this ratio nowhere exceeds unity.

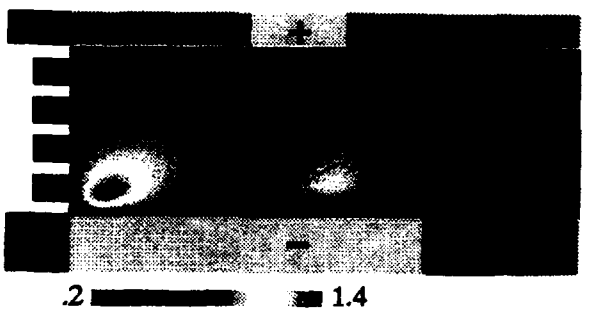

Figure 22: Ratio of ion to electron temperatures for the simulation with anomalous transport ($J = 18$ kA, $\dot{m} = 6$ g/s).

6 Appendix

The elements of the dispersion tensor D_{ij} needed for the calculations carried in this report were derived in refs. [5] and are quoted here for the sake of completeness.

$$D_{11} = 1 + \alpha_i(1 + \zeta_i Z_i) + \alpha_e \left(\frac{1 + \zeta_{e0} e^{-\mu_e} \sum_{n=-\infty}^{\infty} I_n Z_{en}}{1 + i(\nu_e / k_z v_{te}) e^{-\mu_e} \sum_{n=-\infty}^{\infty} I_n Z_{en}} \right) \tag{90}$$

$$D_{12} = -i \frac{\omega_{pe}^2}{\tilde{\omega}^2} \frac{k_z}{k} \zeta_{e0} \sqrt{2\mu_e} e^{-\mu_e} \times \sum_{n=-\infty}^{\infty} (I_n - I_n')(1 + \tilde{\zeta}_{e0} Z_{en}) \tag{91}$$

$$D_{13} = 2 \frac{\omega_{pe}^2}{\tilde{\omega}^2} \frac{k_z}{k} \zeta_{e0} e^{-\mu_e} \times \sum_{n=-\infty}^{\infty} I_n \left\{ \vartheta_n^2 Z_{en} + \left[\left(\frac{u_{de}}{v_{te}} \right)^2 / \zeta_{e0} \right] + (1 + \zeta_{en} Z_{en}) \left(\vartheta_n \frac{k_\perp^2 - k_z^2}{k_\perp k_z} - \zeta_{en} \right) \right\} \tag{92}$$

$$D_{22} = 1 - N^2 + \frac{\omega_{pi}^2}{\omega^2} \zeta_i Z_i + \frac{\omega_{pe}^2}{\tilde{\omega}^2} \zeta_{e0} \mu_e e^{-\mu_e} \times \sum_{n=-\infty}^{\infty} \left[\frac{n^2}{\mu_e^2} I_n + 2(I_n - I_n') \right] Z_{en} \tag{93}$$

$$D_{23} = -i \frac{\omega_{pe}^2}{\tilde{\omega}^2} \zeta_{e0} \sqrt{2\mu_e} e^{-\mu_e} \sum_{n=-\infty}^{\infty} (I_n - I_n') \times \left[1 + \left(\frac{k_z}{k_\perp} \vartheta_n + \zeta_{en} \right) Z_{en} \right] \tag{94}$$

$$D_{33} = 1 - N^2 + \frac{\omega_{pi}^2}{\omega^2} \zeta_i Z_i + 2 \frac{\omega_{pe}^2}{\tilde{\omega}^2} \frac{k_\perp^2}{k^2} \left[\left(\zeta_{e0} - \frac{k_z}{k_\perp} \frac{u_{de}}{v_{te}} \right)^2 + \zeta_{e0} e^{-\mu_e} \times \sum_{n=-\infty}^{\infty} I_n Z_{en} \left(\frac{k_z}{k_\perp} \vartheta_n + \zeta_{en} \right)^2 \right] \tag{95}$$

$$D_{21} = -D_{12}; \quad D_{31} = \frac{k_\perp^2}{k^2} D_{13} \tag{96}$$

$$D_{32} = -\frac{k_\perp^2}{k^2} D_{23} \tag{97}$$

where I_n is the modified Bessel function of the first kind of order n and where we have used the following definitions

$$\zeta_{en} \equiv \frac{\omega + n\omega_{ce} - k_\perp u_{de} + i\nu_e}{k_z v_{te}}; \quad \zeta_i \equiv \frac{\omega - k_\perp u_f}{k v_{ti}}; \tag{98}$$

$$\tilde{\omega} \equiv \omega + i\nu_e; \quad \tilde{\zeta}_{e0} \equiv \frac{\tilde{\omega}}{k_z v_{te}} = \zeta_{e0} + \frac{k_\perp}{k_z}\frac{u_{de}}{v_{te}}; \tag{99}$$

$$\vartheta_n \equiv \frac{k_z}{k_\perp}(\zeta_{en} - \tilde{\zeta}_{e0}); \; Z_{en} \equiv Z(\zeta_{en}); \; I_n \equiv I_n(\mu_e). \tag{100}$$

where Z is the standard plasma dispersion function and where the thermal velocity, plasma frequency and cyclotron frequency of species s are, respectively, given by

$$v_{ts} = (2T_s/m_s)^{1/2}; \; \omega_{ps} \equiv \left(\frac{q_s^2 n_{0_s}}{\epsilon_0 m_s}\right)^{1/2}; \; \omega_{cs} \equiv \frac{q_s B_0}{m_s}. \tag{101}$$

7 Non-technical Material

7.1 Publications supported by the AFOSR Grant

The following four papers from the AFOSR-supported work, listed in the reference list and refered to here with a citation number, have already been published: refs. [4, 38, 27, 28].

A paper entitled "Mass Savings Domain of Plasma Propulsion" by E.Y. Choueiri, A.J. Kelly and R.G. Jahn has been accepted in the Journal of Spacecraft and Rockets and will appear in the issue of October1993.

A paper entitled "Numerical Fluid Simulation of an MPD thruster with a Real Geometry" by G. Caldo, E.Y. Choueiri, A.J. Kelly and R.G. Jahn will be presented at the upcoming International Electric Propulsion Conference in Seattle, September 1993 under paper number IEPC-93-072.

Three papers are currently being prepared for submission to the following three journals: Journal of Plasma Physics, The Physics of Fluids and Journal of Propulsion and Power.

The titles are, consecutively: "Anomalous Transport from a finite-beta collisional instability", "A finite-beta, collisional instability: Theory and experiments" and "Plasma Fluid Simulations of MPD Thruster Flows with anomalous Transport". The authors are: Choueiri, Kelly and Jahn for the first two papers and Choueiri, Caldo, Kelly and Jahn for the last.

Finally the following eight technical reports on work conducted under this grant have been published worldwide by the Mecahnical Aeropsace Engineering Department of Princeton University between Feb 1st 1991 and Feb 1st 1993. They are listed in the reference list and refered to here with a citation number: ref. [39, 40, 41, 42, 43, 44, 45, 46]

7.2 Particpating Professionals

- Dr. Edgar Y. Choueiri, first as a graduate student and research assistant and subsequently as a research associate.
- Dr. Arnold J. Kelly, Senior Research Engineer.
- Dr. Robert G. Jahn, Professor
- Giuliano Caldo, Graduate Student and Research Assistant

7.3 Advanced Degrees

A substantial portion of the Ph.D. thesis of Dr. Choueiri consisted of work conducted under this grant. His thesis[5] bears aknowledgement to AFOSR. His degree was awrded in October of 1991.

A substantial portion of the Masters thesis of Mr. Giuliano Caldo consisted of work conducted under this grant. His thesis is currently in preparation.

7.4 Professional Interactions

We have presented the results of this work at three conferences: International Electric Propulsion Conference 1991, Joint Propulsion Conference 1992 and Symposium on Nuclear Power and Space 1993. We will be presenting some of our final results at the upcoming IPEC conference in September of this year.

7.5 Other Relevant Information

One of the goals we set for this work from the outset is the developement of anomalous transport models that can be easily used by other workers. Although the methodology and derivations are quite complex we have strived toward summarizing the results in the form of compact mathematical formulae. The resulting expressions can be used by the numerical analyst without much detailed familiarity with the mathematics and physics that lay behind the derivations. The detailed documentation offered here and in our publications allow the more interested reader to go deeper in the theoretical aspects of the problem.

We have been transmitting the results of this work to other workers in the field especially to colleagues at NASA Lewis, NASA JPL, Philips Lab at Edwards Air Force Base, MIT, Stuttgart Univresity and the University of Pisa. Some researchers at some of these institutions (e.g. University of Pisa) have already implemented our transport models in their codes and others have told us about their plans to use them in their codes.

Finally, we would like to stress that this work is the first of its kind in plasma propulsion and we believe it has chartered a new territory for the modelling of plasma thrusters. The techniques developed here can be used to address

another important problems of MPD thruster research, most notably the role of turbulence in ionization.

References

[1] E.Y. Choueiri, A.J. Kelly, and R.G. Jahn. MPD thruster instability studies. In 19^{th} *International Electric Propulsion Conference*, Colorado Springs, CO, USA, 1987. AIAA-87-1067.

[2] E.Y. Choueiri, A. J. Kelly, and R. G. Jahn. Current-driven instabilities of an electromagnetically accelerated plasma. In 20^{th} *International Electric Propulsion Conference*, Garmisch-Partenkirchen, W. Germany, 1988. AIAA-88-042.

[3] E.Y. Choueiri, A. J. Kelly, and R. G. Jahn. Current-driven plasma acceleration versus current-driven energy dissipation part I : Wave stability theory. In 21^{st} *International Electric Propulsion Conference*, Orlando, Florida, 1990. AIAA-90-2610.

[4] E.Y. Choueiri, A. J. Kelly, and R. G. Jahn. Current-driven plasma acceleration versus current-driven energy dissipation part II : Electromagnetic wave stability theory and experiments. In 22^{nd} *International Electric Propulsion Conference*, Viareggio, Italy, 1991. IEPC-91-100.

[5] E.Y. Choueiri. *Electron-Ion Streaming Instabilities of an Electromagnetically Accelerated Plasma.* PhD thesis, Princeton University, Princeton, NJ, USA, 1991.

[6] A.A. Vedenov, E.P. Velikhov, and R.Z. Sagdeev. Theory of a weakly turbulent plasma. *Nuclear Fusion*, 1:82–100, 1961.

[7] W.E. Drummond and M.N. Rosenbluth. Anomalous diffusion arising from microinstabilities in a plasma. *Physics of Fluids*, 5(12):1507–1513, 1962.

[8] A.A. Galeev and R.Z. Sagdeev. Theory of weakly turbulent plasma. In A.A. Galeev and R.N. Sudan, editors, *Basic Plasma Physics II.* North-Holland Physics Publishing, Amsterdam, 1984. Part 4.

[9] D.G. Swanson. *Plasma Waves.* Academic Press, Inc., San Diego, 1989.

[10] D.L. Tilley. An investigation of microinstabilities in a kW level self-field MPD thruster. Master's thesis, Princeton University, Princeton, NJ, USA, 1991.

[11] D.L. Tilley, E.Y. Choueiri, A.J. Kelly, and R.G. Jahn. An investigation of microinstabilities in a kW level self-field MPD thruster. In 22^{nd} *International Electric Propulsion Conference*, Viareggio, Italy, 1991. IEPC-91-122.

[12] R.C. Davidson and N.A. Krall. Anomalous transport in high-temperature plasmas with applications to solenoidal fusion systems. *Nuclear Fusion*, 17(6):1313–1372, 1977.

[13] K. Papadopoulos. Microinstabilities and anomalous transport. In R.G. Stone and B.T. Tsurutani, editors, *Collisionless Shocks in the Heliosphere: A Tutorial Review*. American Geophysical Union, Washington, DC, 1985.

[14] R.C. Davidson. *Methods in Nonlinear Plasma Theory*. Academic Press, Inc., New York, 1972.

[15] E.M. Lifshitz and L.P. Pitaevskii. *Statistical Physics, 3rd Edition, Part 1*. Pergamon Press, Oxford, 1980.

[16] D. Winske, M. Tanaka, C.S. Wu, and K.B. Quest. Plasma heating at collisionless shocks due to the kinetic cross-field streaming instability. *Journal of Geophysical Research*, 90(A1):123–136, 1985.

[17] D. Winske, 1991. Los Alamos Natinal Laboratory. Personal communication.

[18] T.K. Fowler. Thermodynamics of unstable plasmas. In A. Simon and W.B. Thompson, editors, *Advances in Plasma Physics*, pages 201–226. Interscience Publishers, New York, 1968.

[19] S.P. Gary and J.J. Sanderson. Energy transport by weak electrostatic drift fluctuations. *Physics of Fluids*, 24(4):638–650, 1981.

[20] C.T. Dum and T.H. Dupree. Nonlinear stabilization of high-frequency instabilities in a magnetic field. *The Physics of Fluids*, 13(8):2064–1081, 190.

[21] D. Hastings and E. Niewood. Theory of the modified two stream instability in an MPD thruster. In 25th *Joint Propulsion Conference*, Monterey, CA, USA, 1989. AIAA-89-2599.

[22] J.B. McBride, E.Ott, J.P. Boris, and J.H. Orens. Theory and simulation of turbulent heating by the modified two-stream instability. *Physics of Fluids*, 15(12):2367–2383, 1972.

[23] J.B. McBride and E. Ott. Electromagnetic and finite-β_e effects on the modified two stream instability. *Physics Letters*, 39A(5):363–364, 1972.

[24] C.S. Wu, Y.M. Zhou, S.T. Tsai, and S.C. Guo. A kinetic cross-field streaming instability. *Physics of Fluids*, 26(5):1259–1267, 1983.

[25] S.T. Tsai, M. Tanaka, J.D. Gaffey Jr., E.H. Da Jornada, and C.S. Wu. Effect of electron thermal anisotropy on the kinetic cross-field streaming instability. *Journal of Plasma Physics*, 32(1):159–178, 1984.

[26] A.D. Gallimore. Thruster anode processes. Contribution to the March/April Bimonthly Progress Report of the Electric Propulsion and Plasma Dynamics Laboratory. Technical Report MAE 1776.30, Electric Propulsion and Plasma Dynamics Laboratory, Princeton University, 1991.

[27] G. Caldo, E.Y. Choueiri, A. J. Kelly, and R. G. Jahn. An MPD code with anomalous transport. In 22nd *International Electric Propulsion Conference*, Viareggio, Italy, 1991. IEPC-91-101.

[28] G. Caldo, E.Y. Choueiri, A. J. Kelly, and R. G. Jahn. Numerical simulation of MPD thruster flows with anomalous transport. In 28th *Joint Propulsion Conference*, Nashville, TN, 1992. AIAA-92-3738.

[29] A.D. Gallimore, A. J. Kelly, and R. G. Jahn. Anode power deposition in MPD thrusters. In 22nd *International Electric Propulsion Conference*, Viareggio, Italy, 1991. IEPC-91-125.

[30] A. Jameson. Transsonic flow calculations. Technical Report MAE 1651, Princeton University, Princeton, New Jersey, 1984.

[31] M. Jayaram and A. Jameson. Multigrid solutions for the Navier-Stokes solutions for flow over wings. In 26th *Aerospace Science Meeting*, Reno, Nevada, 1988. AIAA-88-0705.

[32] R.L. Burton, K.E. Clark, and R.G. Jahn. Measured performance of a multi-megawatt MPD thruster. *Journal of Spacecraft and Rockets*, 20(3):299–304, 1983.

[33] J.H. Gilland. The effect of geometrical scale upon MPD thruster behavior. Master's thesis, Princeton University, Princeton, NJ, USA, 1988.

[34] H. Maecker. Plasma jets in arcs in a process of self-induced magnetic compression. *Z. Phys.*, 141(1):198–216, 1955.

[35] D.D. Ho. Erosion studies in an MPD thruster. Master's thesis, Princeton University, Princeton, NJ, USA, 1981.

[36] R. A. Rowe. Ablation of an MPD thruster. Master's thesis, Princeton University, Princeton, NJ, USA, 1981.

[37] T.M. Randolph, W.F. Von Jaskowsky, A. J. Kelly, and R. G. Jahn. Measurement of ionization levels in the interelectrode region of an MPD thruster. In 28th *Joint Propulsion Conference*, Nashville, TN, 1992. AIAA-92-3460.

[38] E.Y. Choueiri, A. J. Kelly, and R. G. Jahn. Current driven plasma acceleration vesrus current-deiven energy dissipation Part III: anomalous trasnport. In 28th *Joint Propulsion Conference*, Nashville, TN, 1992. AIAA-92-3739.

[39] E.Y. Choueiri. The dispersion tensor of a current-carrying, collisional and flowing magnetoactive plasma. In the January/February Bimonthly Progress Report of the Electric Propulsion and Plasma Dynamics Laboratory. Technical Report MAE 1776.29, EPPDyL, Princeton University, 1991.

[40] E.Y. Choueiri. The satbility of mixed polarization modes. In the March/April Bimonthly Progress Report of the Electric Propulsion and Plasma Dynamics Laboratory. Technical Report MAE 1776.30, EPPDyL, Princeton University, 1991.

[41] E.Y. Choueiri. Wave-particle transport and anomalous dissipation. In the May/June Bimonthly Progress Report of the Electric Propulsion and Plasma Dynamics Laboratory. Technical Report MAE 1776.31, EPPDyL, Princeton University, 1991.

[42] E.Y. Choueiri. Calculations of anomalous transport. In the July/August Bimonthly Progress Report of the Electric Propulsion and Plasma Dynamics Laboratory. Technical Report MAE 1776.32, EPPDyL, Princeton University, 1991.

[43] E.Y. Choueiri. Electromagnetic wave stability theory and experiments. In the September/October Bimonthly Progress Report of the Electric Propulsion and Plasma Dynamics Laboratory. Technical Report MAE 1776.32, EPPDyL, Princeton University, 1991.

[44] E.Y. Choueiri. An introduction to the plasma physics of the MPD thruster. In the November/December Bimonthly Progress Report of the Electric Propulsion and Plasma Dynamics Laboratory. Technical Report MAE 1776.33, EPPDyL, Princeton University, 1991.

[45] E.Y. Choueiri. Anomalous transport models for numerical simulation pf MPD trhuster plasma flows In the January/February Bimonthly Progress Report of the Electric Propulsion and Plasma Dynamics Laboratory. Technical Report MAE 1776.35, EPPDyL, Princeton University, 19^2.

[46] E.Y. Choueiri. Current driven plasma acceleration vesrus current-deiven energy dissipation Part III: anomalous trasnport In the March/April Bimonthly Progress Report of the Electric Propulsion and Plasma Dynamics Laboratory. Technical Report MAE 1776.36, EPPDyL, Princeton University, 1992.